NEUROSCIENCE

Phase coding of spatial representations in the human entorhinal cortex

Zoltan Nadasdy[1,2,3]*, Daniel H. P. Howell[2,4], Ágoston Török[5], T. Peter Nguyen[6], Jason Y. Shen[7,8], Deborah E. Briggs[7,8], Pradeep N. Modur[7,8], Robert J. Buchanan[2,7,9,10]

The grid-like activity pattern of cells in the mammalian entorhinal cortex provides an internal reference frame for allocentric self-localization. The same neurons maintain robust phase couplings with local field oscillations. We found that neurons of the human entorhinal cortex display consistent spatial and temporal phase locking between spikes and slow gamma band local field potentials (LFPs) during virtual navigation. The phase locking maintained an environment-specific map over time. The phase tuning of spikes to the slow gamma band LFP revealed spatially periodic phase grids with environment-dependent scaling and consistent alignment with the environment. Using a Bayesian decoding model, we could predict the avatar's position with near perfect accuracy and, to a lesser extent, that of heading direction as well. These results imply that the phase of spikes relative to spatially modulated gamma oscillations encode allocentric spatial positions. We posit that a joint spatiotemporal phase code can implement the combined neural representation of space and time in the human entorhinal cortex.

INTRODUCTION

The entorhinal cortex (EC) is an integral part of the medial temporal lobe of the mammalian brain and plays a critical role in memory-guided spatial navigation in rodents (1, 2) and in humans (3–6). Grid cells, border cells, and conjunctive head direction cells in the medial EC (mEC), along with place cells and head direction cells in associated areas of the hippocampus and subiculum, are key cellular constituents of the functional network underlying allocentric spatial navigation and enable individuals to localize themselves relative to the environment (7–9). However, grid cells, defined on the basis of the grid-like pattern of their firing rate (FR), account for less than 30% of cells in the rodent dorsomedial EC (2) and less than 25% in the human EC (4, 6). Those cells in the rodent also include conjunctive cells (10). The rest of the neurons (>70%) include head direction cells (58%) (11) and time cells (20%) (10, 12). The network of functionally heterogeneous classes of neurons implies a combined spatial-directional-temporal coding scheme to be prevalent at a cellular level in the EC, yet no such unified code has been identified (13).

Beside their spatial modulation of FR, mEC neurons also exhibit a robust phase tuning relative to intracellular subthreshold oscillations (14, 15) and local field potentials (LFPs) primarily within two harmonic bands: theta and gamma (16). Theta (2 to 12 Hz) and gamma (25 to 60 Hz) oscillations were found to be most prominent during active exploratory behavior and rapid eye movement sleep in rodents (17) and intermittent but still prevalent in the human medial temporal lobe during both real and virtual navigation (3, 18–22).

The spatial periodicity of grid cell activity is also critically dependent on theta band oscillatory drive by the medial septum (23, 24), and inactivation of the septal input was shown to reduce the theta frequency coding of running speed (25). On the other hand, gamma frequency communication between the EC and dentate gyrus underlies spatial and object learning (26). In addition, theta and gamma tend to phase couple in the rodent and human medial temporal lobe (27–30), and both gamma-to-theta and spike-to-theta phase coherence are instrumental for encoding and recall (31–33). Despite the indisputable role of grid cells in the allocentric spatial navigation across the range of mammalian species (2, 4, 6, 34, 35) and the dependency of spatial behavior on theta rhythm, our understanding of the relationship between spatially modulated spike rate, spike phase, and ongoing LFP oscillations during unconstrained two-dimensional (2D) spatial navigation is incomplete, especially in the human brain (15, 36–40).

Efforts to model grid cell properties from the combination of spatial and oscillatory features led to the oscillatory interference model, which explained the emergence of equidistant FR nodes, and a further extension of the model hypothesized that the phase of velocity-controlled oscillations relative to the baseline theta rhythm encodes the distance traveled along a specific direction (41). Elegantly, the same model explained phase precession (42–44). Other models posited that spatial information encoded by the spike phase naturally generates spatially distributed periodic activity patterns as a by-product of the inherent ambiguity of decoding locations from phases (45). However, neither the predicted phase patterns nor allocentric interference patterns have been observed. The challenge was to integrate the phases of spikes over spatial locations and recover the map of phase modulation in two dimensions over the area of the environment. The 1D approach by mapping the phase of spikes relative to theta component of the LFP while the rat is running in a linear track revealed systematic phase precession in the hippocampus (46–48) and in the mediolateral EC (49, 50). However, because the neuronal mechanism of phase precession and the role it plays in encoding space are still debated (51–56), the questions of whether phase coding contributes to the construction of cognitive maps and

the specific frequency band of intrinsic oscillation involved in this coding are still open. Despite various reports of decoding the animal's position and heading direction from theta phase precession of hippocampal place cells (57, 58) or the animal's position from the activity of mEC grid cells (43, 44) during unconstrained 2D navigation, the concept of 2D phase maps (i.e., the spatial distribution of phases) across the entire environment previously only existed in simulations (42–44). Nevertheless, leveraging the theta phase precession using a Bayesian maximum likelihood method afforded moderate decoding performance of the animal's position relative to the center of the place field (57) or the head direction of the animal (58). The common features of these approaches were, regardless of predicting location or direction of the animal, to hinge the decoding on theta phase precession and place cell activity (44, 57–59). On the other hand, previous studies that concerned phase precession in grid cell activity were unable to detect directional or field-specific phase coding (43, 44). A complete empirical 2D reconstruction of phase maps has not been accomplished, neither with respect to theta nor to gamma band LFP.

Since these earlier studies limited the analysis of motion trajectories either by using a linear track (49) or by extracting omnidirectional trajectory segments from the 2D navigation (43), the location-invariant nature of phase coding remained hypothetical (45). Conservation of phase upon unconstrained reentry to a location from different directions, the ultimate proof of phase coding, has not been shown. In addition, earlier experiments did not validate the decoding performance against randomized spike phases dispersed along the actual trajectories to provide an unbiased estimate of decoding. Moreover, although it has long been suggested (46), an allocentric 2D spike phase code across a full environment has never been demonstrated, neither in animals nor in humans. Last, none of the previous studies investigated gamma band LFP as a potential reference for phase coding.

Therefore, we investigated the cellular-level phase coding relative to theta and gamma LFP during unconstrained spatial navigation in 2D environments from the human EC. We were able to derive phase maps to decode the avatar's movement from the phase of spikes, validated the phase decoding against randomized phases, and, lastly, compared the decoding performance between spike phases and FR.

Since spikes of mEC neurons maintain high temporal coherence with local theta and gamma oscillations during locomotion (60), for the same cells to express grid-like spatial periodicity in the environment, a 2D map of the spike to LFP phase coherence must conform with the spatially periodic topography, similar to the FR grids. Given that single-unit activity of the human mEC expresses grid-like firing patterns (4, 6) and the human EC shows intermittent but robust oscillatory LFP both at theta (18, 19, 32) and gamma frequency bands (29, 30), we sought evidence of spatially organized phase maps in data recorded from two patients (subjects 1 and 2) performing spatial navigation tasks in four different virtual environments. These environments were a backyard (BY), a courtyard of the Louvre (LV), a model reconstruction of the main hall of the Luxor (LX) Temple in Egypt, and a large open space (OS) with a boundless horizon and minimal external cues. Both patients in our study underwent intracranial monitoring of epileptiform activity in their medial temporal lobe before the surgical resection of the seizure focus. Because theta frequency modulations correlate with running speed in the rodent and the human (61–63), the walking speed of the avatar in our virtual navigation experiment was set to be constant to eliminate the potential confound of speed affecting the phase of LFP.

RESULTS
Definition of phase maps

Grids of 16 microelectrodes (Fig. 1, A and B) were implanted in the right EC of two previously consented subjects along with different configurations of macroelectrode strips (Table 1). The locations of electrodes were verified by postsurgical magnetic resonance imaging (MRI) and computed tomography (Fig. 1A). We analyzed the single-unit activity (Fig. 1C) from 525 putative neurons isolated with 99% confidence based on their intercluster Mahalanobis distances (64) and verified by >5-ms refractoriness of spike times. LFPs were recorded simultaneously from a separate electrode to rule out contamination of LFP by spike waveforms (Fig. 1B). The two subjects performed spatial navigation tasks in four virtual environments for 30 min each day over seven to eight consecutive days, resulting in a total of 2100 data segments (Table 2). Each data segment was associated with 30 min of navigation in four different virtual environments, spending 5 or 10 min in each. The spike phase analysis was focused on the two most prominent frequency bands of the LFP that significantly deviated from the $1/f$ spectral function: 2 to 2 Hz and 25 to 35 Hz (slow gamma). We identified the former as theta and the latter frequency range as slow gamma or gamma for short (Fig. 1D and fig. S1) (13). Building on previous findings (4, 6, 13) of grid cells expressing allocentric spatially periodic firing patterns in humans (Fig. 1, F and G) while maintaining firing phase coherence with LFP [including phase precession (65)], we hypothesized that average aggregate spike phases should unravel spatially periodic patterns when resolved in the 2D space of navigation (Fig. 1H). Although our analysis was agnostic to the frequency band of the LFP, the theta and gamma frequency band LFP references generated different maps from the same spike train. To determine the optimal frequency band to serve as reference, we compared the temporal stability of the resulting phase maps between theta and gamma band LFP. Furthermore, we were also aware that spike trains may not reveal consistent phase maps beyond the by-chance joint probability of spatial and temporal patterns.

To determine the phase of spikes, we first bandpass-filtered the wide-band LFP at theta (2 to 12 Hz) and gamma (25 to 35 Hz) frequency bands and then computed the Hilbert transforms of the filtered signals separately (Fig. 1E). The Hilbert transforms of LFP defined the instantaneous phases of spikes relative to theta and gamma band LFP with less than 1° resolution at 1-ms sampling frequency. The 1-ms precise intersections of spike times with the two phase transforms defined two phase vectors converting the spike times to spike phases (ϕ), one vector relative to theta and the other vector relative to gamma, referred herein as gamma phases and theta phases, respectively (Fig. 1E) (13). While the distributions of spike phases for most cells were nonuniform, three times as many (19%) neurons expressed deviation from uniform phase distribution relative to gamma as to theta (6.21%) [Fig. 1I and figs. S3 and S6E; Rayleigh$_{(gamma)}P < 0.05$: 94 of 478 cells or 376 of 1914 epochs; binomial test, $P = 2.3066 \times 10^{-43}$ and Rayleigh$_{(theta)}P < 0.05$: 23 of 370 cells or 92 of 1480 epochs; binomial test, $P = 0.0274$] and 10 times as many ϕ with Rayleigh$_{(gamma)}P < 0.01$. Moreover, the average single-unit ϕ, examined individually or combined across electrodes 1 to 4, displayed notable polarization relative to gamma [Figs. 2B, 3 (A to E), and 4 (A to D, third column) and figs. S3 and S9J] but distributed uniformly relative to theta (Figs. 3F and 4E, third column; Rayleigh P values are indicated above the circular histograms).
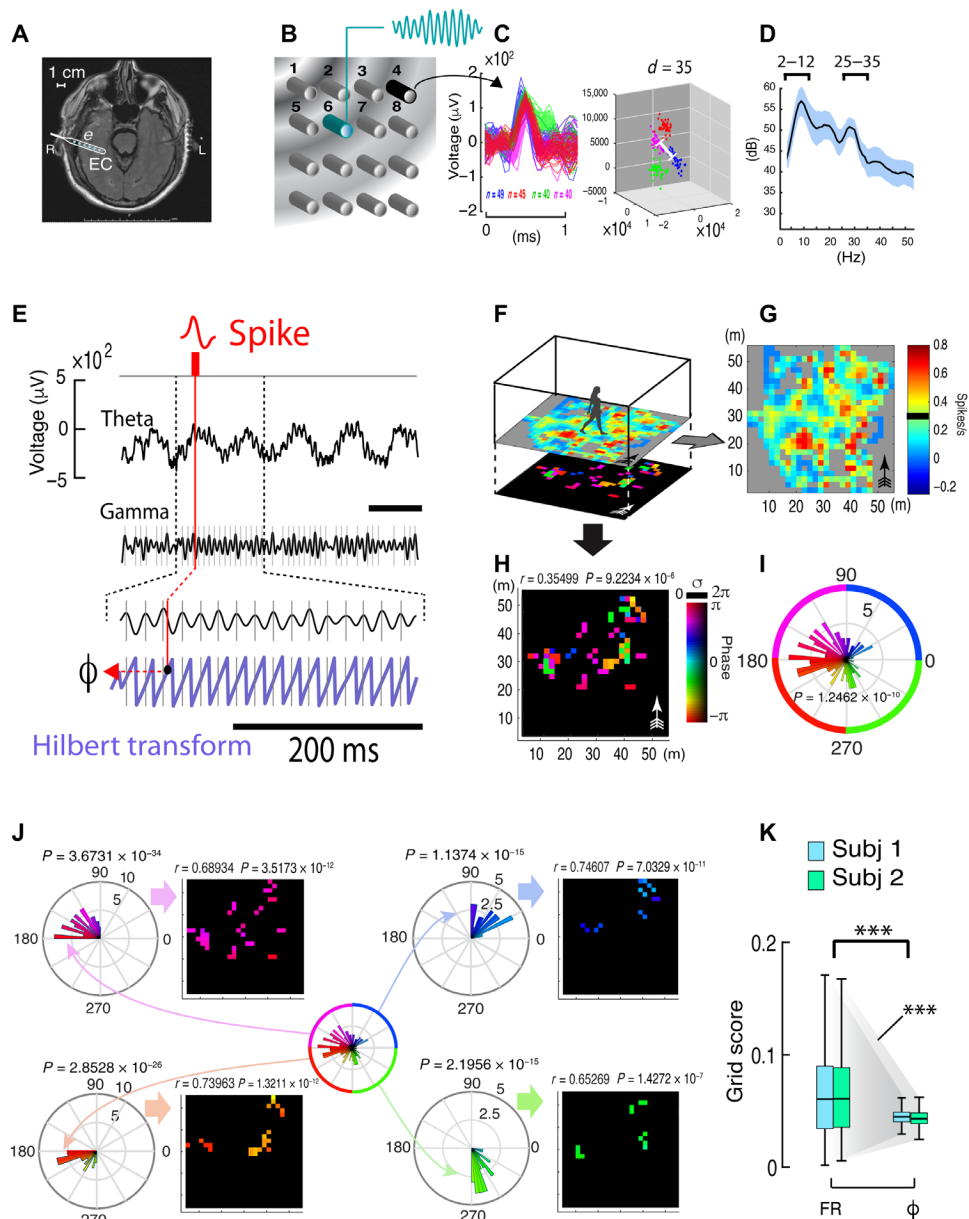
Fig. 1. Construction of phase maps. (**A**) Postsurgical MRI verification of the electrode position in the right EC. The electrode strip (*e*) is accentuated. (**B**) Schematic of the 4 by 4 microelectrode grid (interelectrode spacing is 1 mm). A designated electrode (#6) served as the source of LFP, while other electrodes recorded single-unit activity. Circular waves illustrate propagating gamma waves. (**C**) Spike waveforms and clusters extracted from 20 min of data with the shortest intercluster Mahalanobis distance indicated. (**D**) Average spectral density of LFP sampled at 2 to 50 Hz during a 10-min spatial memory task. The two most prominent frequency components at theta (2 to 12 Hz) and slow gamma (25 to 35 Hz) are labeled (shaded area represents SEM). (**E**) Computation of phase of spikes relative to LFP (1-s data). From the top: spike event, broad-band LFP (bandpass filtered, 0.1 to 300 Hz) displaying theta-modulated gamma oscillations, and gamma LFP (bandpass filtered, 25 to 35 Hz) and its Hilbert transform (purple trace). The phase of a spike is defined by the intersection of spike time (red line) with the Hilbert transform (red arrow) of the bandpass-filtered LFP. (**F**) A 3D representation of the mean FR map overlaid on the mean phase map (bin size = 4 virtual $\bar{m}^2$) and their respective orthogonal views (**G** and **H**). For phase maps, the hue and luminance correspond with mean phase and variance of phase, respectively. (**I**) Radial histogram of spike phases (φ) relative to gamma LFP combined and (**J**) separated according the four quadrants of the phase spectrum. The *r* and *P* values correspond to Pearson's correlation coefficients between phase and avatar's trajectory and their significance. (F and J) Plots are based on recording of one cell in one environment. (**K**) Comparisons of grid scores between FRs and gamma phases (φ) by combining all data from two subjects (blue and green represent subjects 1 and 2, respectively). ***$P < 0.001$.

To elucidate the spatial distribution of φ, we binned the area of each virtual environment into uniform size proportionate square units (.7 by .7, 2 by 2, and 3 by 3 $\bar{m}$, where $\bar{m}$ is virtual meter) and computed the circular mean and circular variance of φ over the visited units [equivalent of computing the resultant vector of φ (*48*)].

By integrating φ over the visited areas, we computed a variance-weighted spatial distribution of phases ("phase map" hereinafter) denoted by Φ (Figs. 1H and 2C) (*13*). Moreover, we computed traditional FR maps (Figs. 1G and 2A), phase tuning histograms (Figs. 1I and 2B), maps of mean heading direction denoted by ρ

Table 1. Patients' data, diagnoses, and recording information.

Patient no.	Diagnosis	Symptoms	Hemisphere of seizure origin	Dominant Hemisphere	Electrode implantation	Number of recording days
Subject 1	Multifocal epilepsy due to cavernous angiomas in the right mesial temporal lobe and in the inferior aspect of the right frontal lobe.	Intractable seizures	Right	Left	An array of subdural electrodes over the right convexity temporal lobe and EC. Bilateral hippocampal depth electrodes.	8
Subject 2	Multifocal epilepsy	Intractable seizures	Right	Left	An array of subdural electrodes over the right convexity temporal lobe and EC. Bilateral hippocampal depth electrodes.	7

Table 2. Dimensions and features of the virtual environments. N/A, not applicable.

Environments	Size (m)	Area (m^2)	Bin size (m)	Shape	Boundaries	Obstacle	External cues	Topology (roof)
BY	18 by 18	324	.7 by .7	Square	✓	None	✓	Open
LV	50 by 70	3500	2 by 2	Rectangle	✓	None	✓	Open
LX	52 by 52 by 10	2704	2 by 2	Square	✓	✓	✓	Closed
OS	(70 by 70)*	4900	3 by 3	N/A	None	None	Spaceships	Open

*The OS environment did not have visible boundaries, nevertheless above dimensions apply to the navigable area.

(Fig. 2D), the resultant vector length (RVL) of the heading direction, and the correlation of Φ with heading direction and with RVL from daily navigation sessions for each cell in four different environments (Fig. 2E and fig. S7, fourth column). According to these correlations, most cells expressed strongly nonuniform phase distributions, clustered heading directions to phase relationship (Fig. 2E, "BY" environment, and fig. S7) and occasional dependency of phase ϕ on heading directions ($P_{\chi 2} < 0.0001$; Fig. 2E, "LV" environment; and figs. S7, A and C, and S8, A to E).

Despite the large positional and directional variability of trajectories within and across environments, the Φ phase maps revealed environment-aligned periodic clusters of iso-phase densities with smooth phase transitions between clusters (fig. S11). The stability of iso-phase clusters was tested by cross-validation (fig. S5). The patterns of iso-phase nodes resembled those of grid cell FR maps (2). The spatially periodic pattern was prevalent even if the cell's Φ grids did not coregister with the FR grids (Figs. 1, G and H, and 2, A and C). The composition of iso-phase nodes in Φ was consistent with a grid-like pattern expressing a constant spatial shift between Φ nodes after decomposition of ϕ according to phase quadrants (Figs. 1J and 2C and fig. S10, C, E, and F). Moreover, phase grids displayed sharper clusters than FR grids as the variance of grid scores computed from the Φ-values of all cells was significantly smaller than those computed from FR maps [coefficient of variation $CV_{FR-gridmod} = 0.5997$ and $CV_{phase-gridmod} = 0.2623$ and

two-way analysis of variance (ANOVA): $F_{subject} = 0.73$, $P_{(1,2094)} = 0.3917$ and $F_{FR, \phi} = 143.02$, $P_{(1,2094)} = 0.00097$; Fig. 1K].

## Environment-dependent scaling of phase maps

To examine the environmental dependence of Φ, we calculated the average distance between iso-phase nodes (Fig. 2C) within each environment across the six to nine sessions played per subject and found a monotonic increase of iso-phase distances with the size of environments (Fig. 2, F to H; BY = 5.462 m̄, LX = 15.812 m̄, LV = 18.242 m̄, and OS = 19.119 m̄). Although the FR grids did not necessarily coregister with the iso-phase nodes of Φ, as mentioned earlier (Fig. 2, A to C), the average iso-phase distance and its scaling with the size of the environment were consistent with the FR grid scaling (Fig. 2, F and H) (6, 13). The average iso-phase distance scaled linearly with the size of the environment ($\sqrt{ab}$) [Fig. 2G; subject 1: R^2 (coefficient of determination) = 0.5448, root-mean-square error (RMSE) = 4.711, $f(x) = 0.2835x + 0.669$; subject 2: $R^2 = 0.2026$, RMSE = 7.395, $f(x) = 0.1834x + 3.087$]. The slope of iso-phase grid scaling (0.2835 and 0.1834) was slightly smaller but comparable to the slope of FR grids (subject 1 = 0.4108 and subject 2 = 0.3509; Fig. 2H) (6, 13).

Because of the low FRs of cells (<1 Hz for $n_{[0...1\ Hz]} \geq 80\%$ of cells), most of the EC neurons generated sparse phase maps (Figs. 3, B to E, and 4, B to D; and fig. S4). To increase the spatial coverage of these neurons and unravel the spatial pattern of Φ
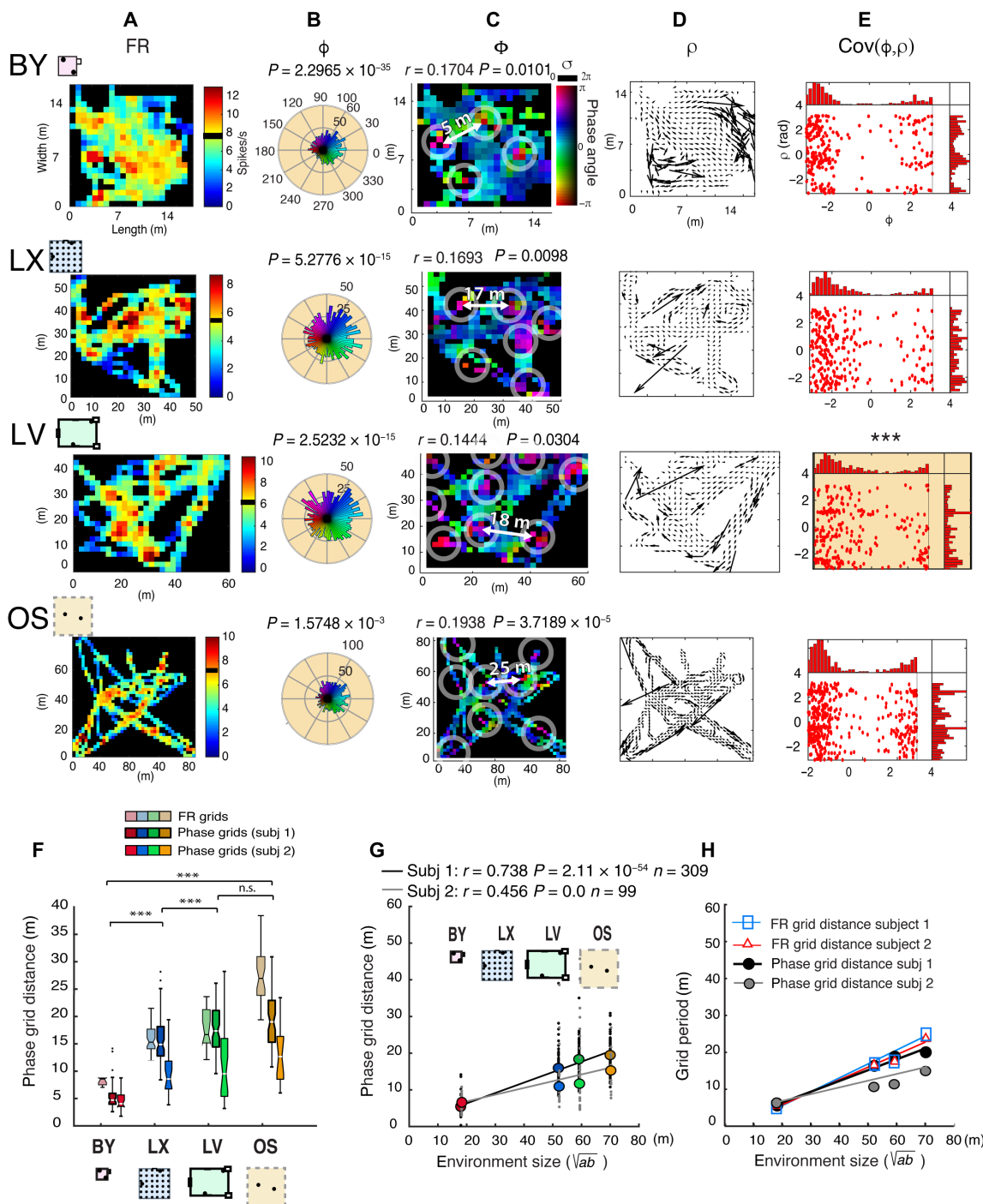
Fig. 2. Environment-dependent scaling of phase maps. (**A**) FR maps of a combined set of single units ($n = 4$) monitored in four different virtual environments (BY, LV, LX, and OS). The axis scaling in virtual meters ($\bar{m}$) reflects the dimension of environments. Black horizontal lines on scale bars indicate mean FR. (**B**) Polar histograms of gamma phase tuning (ϕ) of combined unit activity per environment. P values represent the significances of Rayleigh tests for circular nonuniformity. (**C**) Variance-weighted gamma phase maps (Φ described in Fig. 1). The r values represent correlation coefficients between gamma ϕ and RVL of heading, along with the corresponding P values. Circles highlight near-π (purple) iso-phase nodes close. Iso-phase distances are indicated. (**D**) Local RVL and ρ of heading directions. Larger arrows represent smaller variance. (**E**) Heading direction (ρ) and gamma ϕ covariance. Red symbols depict the local heading direction ($-\pi < \text{dir} < \pi$) as a function of ϕ. Histograms capture the marginal distributions. Asterisks above the plot indicate the nonindependence of phase and heading direction ($\chi^2 = 107.5121$, $P = 0.0005$). (**F**) Comparison of FR grid and Φ grid scaling across environments. The boxplot triplets from left to right represent the distribution of mean distances between FR grid centers and mean distances between iso-phase grid centers for subjects 1 and 2 (boxes represent the median, 25th, and 75th percentile of the data). Color rectangles depict scale proportional layouts of the four environments. (**G**) Phase grid scaling as a function of environment size in virtual meters ($\bar{m}$) (subjects 1 and 2). Pearson's correlation coefficients between iso-phase distance and environment sizes are indicated. (**H**) Comparison of slopes of the environment-dependent scale functions of Φ relative to FR grids. (A to E) Examples from a single subject in the same day in four different environments. (F to H) Population data from both subjects over all days and environments combined.
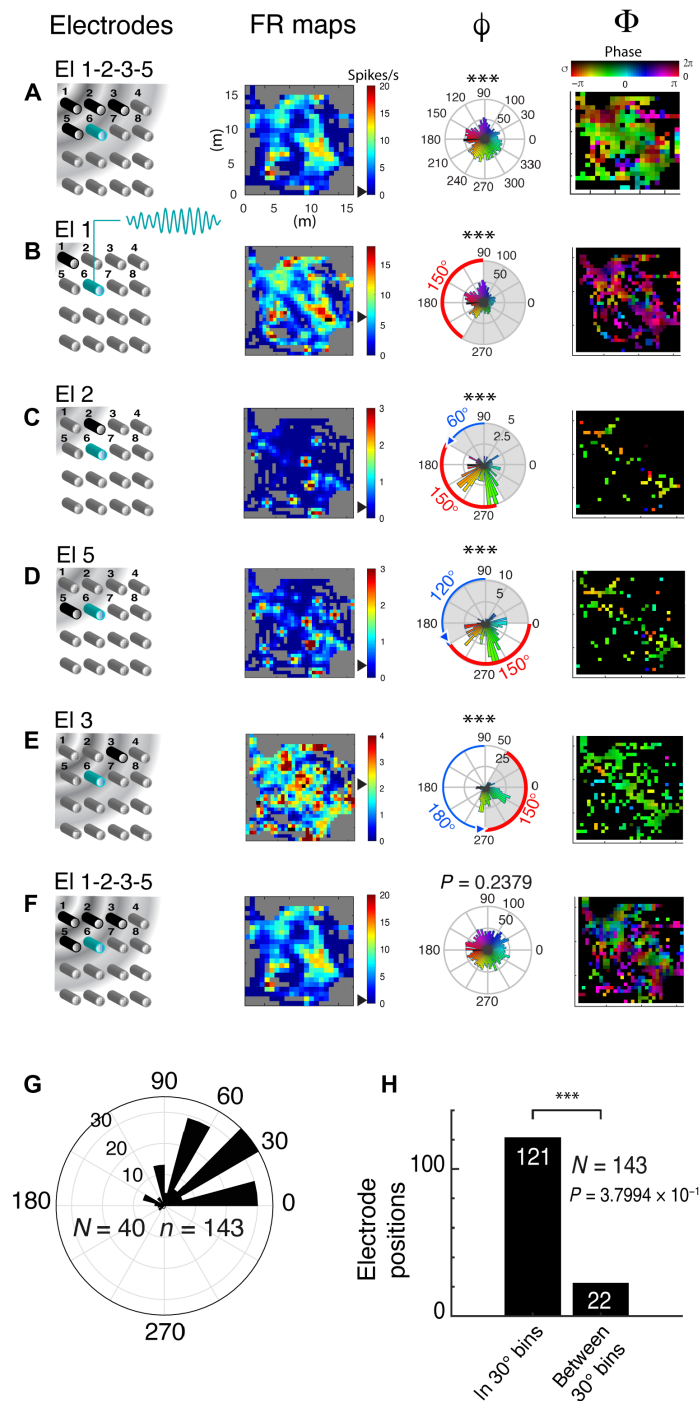
Fig. 3. Dependence of spike phase on electrode position. (**A** to **F**) FR maps and phases of single units grouped by electrodes (examples from a single environment from one subject and 1 day over multiple electrodes). Phases were computed relative to gamma (A to E) and theta (F). (A and F) Spikes combined over four electrodes ($n = 2908$ spikes). (B to E) Units combined over single electrodes. Electrode position varied. First column: Spatial configurations of the microelectrode grid. Gray shading illustrates the theoretical gamma phase difference between electrodes. Second column: FR maps. Arrowheads on scale bars represent average FRs. Third column: Polar histograms of ϕ relative to gamma LFP, except that (F) is relative to theta. Blue angles represent a constant rotation of ϕ between electrodes, and red angles signify the angular span of the phase distribution. Fourth column: Spatial phase maps (Φ) relative to gamma and theta (A to E and F, respectively). Local mean phase and phase variance are represented by colors and darkness, respectively. Asterisks above ϕ indicate the significance of the Rayleigh test of directionality; under ϕ heading represent χ^2 test of phase RVL covariance. (**G**) Summary of phase rotation. Polar histogram represents the interelectrode rotation angles combined over days and sessions from both subjects between electrode pairs. (**H**) Bar chart represents the difference between counts of rotation angles between electrode pairs when the angles fall within bins defined as integer multiples of 30° and between those. P value indicates the significance of the binomial test between the two counts. (A to F) Examples from one subject, 1 day, one environment, one electrode, and different units. Spatial dimension of pixels is 0.7 by 0.7 m̄. P values of polar histograms under ϕ represent the Rayleigh test of directionality. The polar histograms were binned by 5°, and phase maps and average velocity maps were binned by 0.7 by 0.7 m̄ bins.
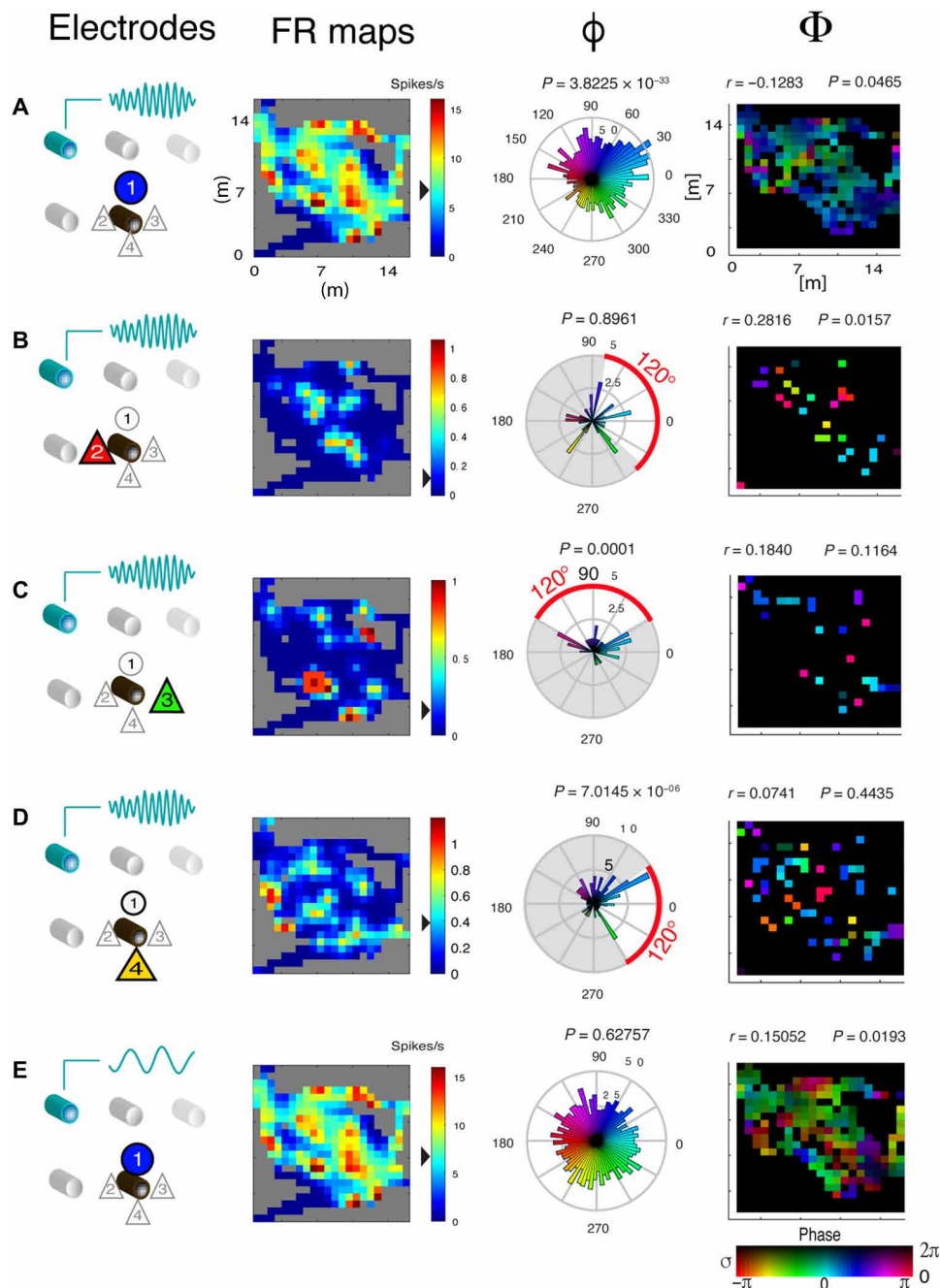
Fig. 4. Dependence of spike phase on single-unit identity. (**A** to **E**) Phase differences across single units isolated from the same electrode with respect to gamma (A to D) and theta (E). First column: Schematics of putative single neurons recorded from 1 of the 16 microwire electrodes. Second to fourth columns: Same as in Fig. 3, except that φ and Φ represent the activity of individual neurons isolated from the same electrode. Red angles under φ indicate differences in phase between discrete phase tuning modes. Color and darkness in Φ represent phase and variance, respectively, as in Figs. 1 to 3. (All examples were recorded simultaneously from one subject, 1 day, one environment, one electrode, and different units. Same subject and same environment as in Fig. 3 but different day and electrode.) Spatial dimension of pixels is 0.7 by 0.7 m̄. P values of polar histograms under φ represent the significance of Rayleigh test of directionality. The polar histograms were binned by 5°, and phase maps and average velocity maps were binned by 0.7 by 0.7 m̄ bins.

despite low FR units, we merged the spike times of 16 putative neurons (four units from four electrodes) before computing the average phase map that evolved during each 5-min navigation session and compared that with the phase maps of individual single units. The angular distribution of gamma or theta phases φ across all spatial locations was typically uniform when combined across all four electrodes during 5-min navigation in a given environment (Rayleigh $P > 0.05$; Fig. 2B and fig. S4A). In contrast, the same set of neurons displayed highly polarized spatial distributions of Φ when the phases were displayed in the 2D area of virtual navigation (Fig. 2C

and fig. S4A, third column), regardless of the choice of LFP reference gamma or theta (Fig. 3, A and F). Whether the topography of the Φ is stable in the given environment or changing over time is crucial for the reliability of allocentric spatial representations. The stability of Φ maps over time and their robustness to spike sampling were tested using two independent cross-validation methods, blockwise and subsampling, each applied to a 5-min interval of game playing (fig. S5, A, B to D, and E to G). The correlations between the subsampled spikes confirmed the stability and robustness of phase maps to spike sampling [Pearson's $r = 0.403$, $P_{(1,359)} < 0.0001$ and $r = 0.239$, $P_{(1,359)} < 0.0001$ for stability and robustness, respectively].

Phase maps are different from by-chance phase coincidences

To test the statistical significance of spatial organization of Φ against by-chance pattern formation and to elucidate the feature that controls the topography of phase maps, we applied two types of surrogate tests: interspike interval (ISI) shuffling and phase permutation of the LFP (fig. S6, A to C). Both types of surrogate spike trains retained the average FR and the original ISI histograms of neurons. At the same time, both methods effectively eliminated any systematic temporal relationship between spikes and LFP. Although the 2D entropy of Φ and its correlation with navigation were immune to the ISI shuffling, entropy increased, and behavioral correlation decreased after phase permutation of LFP (Table 3). The concordance of the two results suggests that the spatial pattern of the LFP phase, as a 2D projection of the collective membrane potential oscillation dynamics, may effectively control the spike timing of grid cells.

Next, we compared the spatial organization of Φ between gamma and theta with respect to entropy, prominence of low spatial frequency components of phase autocorrelograms, and the correlation of phase maps with the avatar's movement directions in space. Although both theta and gamma Φ-values displayed equally high correlations with the avatar's movement directions [Kruskal-Wallis test, $P = 0.4528$, $r_{(\Phi, \text{dir})} > 0.5$, $P_{(\Phi, \text{dir})} > 0.0001$], gamma Φ displayed a significantly higher-order spatial structure (smaller entropy) and larger power in the low-frequency spatial harmonics than theta Φ (Kruskal-Wallis tests, $P_{\chi 2} < 0.0001$; fig. S6D and Table 4).

Phase relationship between distant groups of neurons

In all previous examples, we combined single-unit activity across electrodes to increase the spatial coverage of neuronal activity and elucidate the phase maps in their entirety (fig. S4). However, by doing so, the contribution of single cells to the average phase maps remained obscured by the contribution of the entire cell population. To tease apart the effects of single neurons to the average phase map, we compared Φ across different electrodes and across individual neurons isolated from the same electrode. First, we identified a recording from a single 5-min session of one environment from one subject and day where we could isolate 16 single-unit spike trains from four different electrodes (four neurons per electrode) and investigated the phase composition of ϕ-values and Φ-values by merging the spike trains at the electrode level. The phase was computed relative to gamma and theta LFP, where the LFP was always recorded from a separate electrode to ensure that the phase and frequency of LFP were uncontaminated by the harmonic components of single-unit activity (Fig. 3, A to F, and figs. S7 and S8). When electrodes and units were combined, the ϕ polar histogram displayed a highly nonuniform phase distribution (Rayleigh $P < 0.001$; Fig. 3A). Despite the moderate FR gridness scores ($g = 0.014$, $P > 0.05$), the

gamma Φ expressed strong periodicity in alignment with the environment (Fig. 3A). Comparisons of phase differences (β_{ij}) between pairs of electrodes 1 and 2, 1 and 5, and 1 and 3 revealed a rotation series of 60°, 120°, and 180° rotation of phases (Fig. 3, B and C, B to D, and B to E), respectively. Hence, the phase spectrum rotates with 60° increments with every electrode position as the Euclidean distance increases between the electrodes, whereas the 150° span of the phase tuning was invariant to the electrode position (Fig. 3, B to E, and fig. S7, red angles). Notably, the observed phase tuning was specific to gamma band LFP (Rayleigh $P < 0.001$; Fig. 3, A to E). On one hand, the distance-dependent rotation of ϕ suggests a spatially nonlinear but constant interelectrode delay of gamma phases, which is consistent with a propagating gamma fields dynamics (Fig. 3, first column), also evident from the delayed correlation analysis of gamma and theta between electrode pairs (figs. S1 and S2). On the basis of the known interelectrode distance, the angle of phase rotation, and the predefined gamma frequency, the speed estimate of gamma field propagation was between 0.135 and 0.189 mm/ms. To demonstrate that the discrete and constant phase rotation between electrodes was not an isolated example, we combined the phase rotations between pairs of electrodes where the two phase distributions allowed for unambiguous identification of the corresponding peaks and histogrammed them with 15° bins (Fig. 3G). The polar histogram revealed a discrete sequence of angles that represent integer multiples of 30° phase rotations, consistent with the propagation delay between electrode pairs of the evenly spaced multielectrode grid. The interelectrode phase rotations of 30°, 60°, or 90° between electrodes were reproducible across virtual environments, days, and subjects with very few exceptions (binomial test, $P < 0.00001$; Fig. 3H). Moreover, the gamma phase of combined single-unit activity on each electrode expressed a significant dependency on the avatar's heading direction (χ^2 test, $P < 0.05$), but no similar relationship was observed between heading and theta phases (χ^2 test, $P = 0.1157$) (fig. S8F, rightmost column).

Phase relationship between nearby neurons

Next, we examined the contribution of individual neurons to the average phase composition of a group of neurons recorded from the same electrode over a 5-min duration of navigation in one environment (Fig. 4, A to E). Single units were verified by their high isolation coefficients [Mahalanobis distance between nearest clusters $d_{n > 50} \geq 20$ corresponds with >99% confidence (6, 13, 64)] and >5-ms refractory period in their ISI histograms. The second column of fig. S8 represents typical examples of single-unit ϕ-values isolated from a group of neurons simultaneously recorded from the same electrode, each displaying highly polarized phase tuning. The first neuron displayed a strong 30° polarity with relatively high FR (mean = 7 spikes/s, Rayleigh $P < 0.0001$; Fig. 4A, ϕ). The second neuron with low FR (mean = 0.1 spikes/s) displayed five equiangular phases with 72° rotational symmetry (Rayleigh $P = 0.8961$; Fig. 4B, ϕ). Whereas the other two neurons displayed only two components of the pentangular phase tuning, one with 144° and another with 72° between the peaks, both of these neurons' phase tuning histograms were highly polarized (Rayleigh $P \leq 0.0001$), conformed with the fivefold symmetry (Fig. 4, C and D, ϕ and Φ), and retained a precise coregistration with firing phases of all the other cells from this electrode. The highly polarized ϕ, typical of gamma LFP, was in stark contrast with the lack of phase tuning expressed with respect to theta

Table 3. The statistics of surrogate analysis. Nos. 1 and 2 are the difference between original and ISI-permuted dataset and between original and phase-randomized LFP dataset with respect to the correlation between phase and resultant vector length (RVL) of movements. No. 3 represents the medians of data per datasets (from left to right) in the original dataset and the ISI-permuted LFP and phase-permuted LFP datasets separately for subject 1 and subject 2. Nos. 4 and 5 represent the entropy difference between the original and ISI-permuted datasets and between the original and phase-randomized LFP datasets. No. 6 contains the median entropy values of original data and ISI-permuted LFP and phase-permuted LFP datasets. Nos. 7 and 8 represent the statistical difference in the low-frequency power of the 2D spectrum between the original spatial phase and the ISI-permuted phase and between the original spatial phase and phase-randomized LFP phase patterns. No. 9 lists the median power corresponding to the low-frequency power of original and ISI-permuted LFP and phase-randomized LFP datasets.

No.	Test	Variable	P	Ha P < 0.05	zval	n	P	Ha P < 0.05	zval	n	Supplementary figure
1	Rank sum	PH-VELO-ISI	0.5348	0	−0.6207	910 910	0.8165	0	0.2321	1004 1004	fig. S6A
2	Rank sum	PH-VELO-REVLFP	0	1	10.5241	910 909	0	1	7.8262	1004 1003	fig. S6A
3	Medians		0.4982	0.5046	0.3965		0.5575	0.5586	0.4905		
4	Signed rank	PH-GRID-ENTR-PHGRID-ENTR-ISI	0.7487	0	0.3204	910	0.3619	0	0.9118	1004	fig. S6B
5	Signed rank	PH-GRID-ENTR-PHGRID-ENTR-REVLFP	0	1	−10.51	910	0.0026	1	−3.0143	1004	fig. S6B
6	Medians		0.1544	0.1525	0.1621		0.0923	0.1	0.1015		
7	Signed rank	PH-GRID-POWER-PHGRID-POWER-ISI	0.0072	1	2.6879	697	0	1	11.8777	1004	fig. S6C
8	Signed rank	PH-GRID-POWER-PHGRID-POWER-REVLFP	0.0956	0	1.6668	697	0	1	8.6097	1004	fig. S6C
9	Medians		0.0551	0.0532	0.0544		0.0821	0.0654	0.0708		

Table 4. The Kruskal-Wallis nonparametric ANOVA of theta to gamma phase map comparison. Data from the two subjects were combined. First row: Comparison of spike phase to heading direction correlations between spike phases derived from gamma versus theta oscillations showed no significant difference. Second row: Kruskal-Wallis test comparing gamma and theta phase maps with respect to entropy indicated significantly lower entropy for gamma phase maps. Third row: Kruskal-Wallis test comparing the power of low-frequency components of the 2D spectra between gamma and theta phase maps indicated significantly larger low-frequency power in the gamma phase maps.

No.	Statistics	Theta-gamma	df	n	χ^2 test	P	Sign	Supplementary figure
1	Kruskal-Wallis	Phase heading r	1	3396	0.5637	0.4528		fig. S6D, left
2	Kruskal-Wallis	Entropy e	1	3396	24.3	8.24×10^{-7}	***	fig. S6D, middle
3	Kruskal-Wallis	Low-frequency power	1	3396	41.61	1.12×10^{-10}	***	fig. S6D, right

(Fig. 4E). Despite the dispersed spatial scattering, each cell maintained the association of iso-phase nodes with spatial locations relative to the environment (Fig. 4, A to D, Φ). Although theta ϕ was homogeneously distributed across the phase spectrum (Rayleigh $P = 0.627$), it displayed a clear dependency on the direction of heading [χ^2 test, $P_{(n = 196)} = 7.3819 \times 10^{-6}$; Fig. 4E, ϕ heading].

In summary, distant groups of neurons show a distance-dependent rotation of their phase spectrum, while the shape of the phase spectrum does not change (Fig. 3, A to E, and fig. S12A). In contrast, individual neurons within the same local assembly display discrete

equiangular phase distributions with preserved absolute angle of peaks but different prominence of certain angles (Fig. 4, A to D, and fig. S12B). These two observations suggest that while the absolute phases of the group of neurons cannot encode information, the phase difference between neurons potentially could. If gamma oscillations manifest as traveling waves through the EC, then the absolute phase of spikes has no physiological meaning because it depends on where we measure gamma, except when taking the neuron's own subthreshold gamma oscillation as a reference. However, the relative spike phase differences between neurons are maintained across the

population regardless of the actual phase of the gamma field. Therefore, the next question we address is whether we can decode the spatial information from the relative phase differences between neurons.

Decoding positional information from phase

If the phase of spikes relative to gamma encodes allocentric localization information (position and/or direction), then given that the same gamma oscillation is shared with downstream neurons, it follows that they can decode the avatar's position/direction from the phase itself as precisely as our subjects were able to localize their avatar in the virtual environment. However, because of the spatial periodicity of phase maps, multiple locations can be associated with a given gamma phase. To reduce the ambiguity of localization, our goal was to use the avatar's actual position at a time of the spike for predicting the impending spatial position at the next spike ($x_{\text{spike}i+1}$, $y_{\text{spike}i+1}$) and the heading direction ($\alpha_{\text{spike}i, i+1}$) within the neighborhood defined by the 20 forthcoming spikes $x_{k \in i1...20}$, $y_{k \in i1...20}$ (fig. S13, C to F). Although the decoding was performed relative to the previous spike, both (α) and position (x, y) estimates were computed in environment-referenced, allocentric coordinates (fig. S13, E and F). Following the Bayesian decoding framework, we used the actual position of the avatar at the time of a predicate spike (x_0, y_0), the phase of the next spike ϕ_1, the phase probability map Φ, and the probability of the avatar being at that position $p_{A(x, y)}$. The goal of decoding was to predict the position of the subsequent spike (x_1, y_1) from the phase ϕ_1 given Φ and $p_{A(x, y)}$. We captured the direction decoding errors in a circular histogram (fig. S13G) and in a form of a confusion matrix (CM) (fig. S13H), comprising the predicted positions or directions as a function of observed positions or heading directions of the avatar, respectively. To increase the spatial density of spikes for reliable spike phase estimates of Φ^{prior}, we combined the spikes across all neurons and electrodes but kept the days and navigation sessions (environments) separate. To ensure that the gamma component of the LFP was uncontaminated by the spikes, we recorded the LFP and the spikes from different electrodes separated by at least 1 mm. For decoding the avatar's position or direction from the phase of spike, we sought to determine the spike with the maximum likelihood arg max ($p(\phi_T | x, y)$), where (x, y) was the estimated allocentric coordinate. The tangent of the shortest Euclidean path between successive spike positions relative to the opposite and adjacent walls provided the heading direction as $\alpha = \tan^{-1}(dx/dy)$ of the avatar, where $dx = x_1 - x_0$ and $dy = y_1 - y_0$. We iterated the process for every spike in the test set per session and computed the average CM for each session and day (fig. S13H). The mean decoding error matrices of direction [$\alpha_{(\text{error})}$], positions [$x, y_{(\text{error})}$], and path lengths [$l_{(\text{error})}$] were averaged across environments and days, but the two subjects' data were kept separated (Fig. 5). Correlations between decoded and actual movement parameters including heading direction, position, and path length were all significant (circ $r_{\text{dir}} = 0.347$, $P < 0.001$ and circ $r_{\text{dir}} = 0.332$, $P < 0.001$ for subjects 1 and 2, respectively; $r_{\text{pos}} = 0.838$, $P < 0.001$ and $r_{\text{pos}} = 0.688$, $P < 0.001$ for subjects 1 and 2, respectively; $r_{\text{length}} = 0.714$, $P < 0.001$ and $r_{\text{length}} = 0.625$, $P < 0.001$ for subjects 1 and 2, respectively). Representative decoding performances are illustrated in Fig. 5 (A and B, insets) and fig. S14. Nevertheless, to compensate for the decoding bias deriving from the narrow dispersion of spikes along straight trajectories, we applied two interventions. First, we excluded straight movement trajectories from the analysis by limiting the analysis to $r < 15 \bar{m}$, where r is the radius of path curvature. Second, we computed a CM [$M_{(\text{Null})}$] using the original spike time data and movement trajectory but shuffled

the spike phases across the spikes and subtracted the shuffled phase CM M_{Null} from the observed phase CM M_{obs} for directions [$\alpha_{(\text{error})}$] and for positions $x, y_{(\text{error})}$ separately (Fig. 5, A and B). The corrected CMs retained a near-perfect decoding performance for allocentric positions (Fig. 5B; Pearson's $r_{\text{subj1}} = 0.3220$, $P = 0.005$ and $r_{\text{subj2}} = 0.1957$, $P = 0.0046$, and areas under receiver operating characteristic (ROC) curves for both subjects were above 0.99; Fig. 5D and see fig. S15 for the construction of ROC curves) but partly lost predictability for directions (Fig. 5A; $r_{\text{dir}} = 0.092$, $P = 0.0001$ and $r_{\text{dir}} = 0.037$, $P = 0.120$ for subjects 1 and 2, respectively) as also evident from the differential dispersion of the distributions of CMs. At the same time, the diagonal distribution of the true phase CM was narrower than that of the phase-shuffled Null for data from both subjects (Kolmogorov-Smirnoff test after Benjamini-Hochberg correction for multiple comparisons).

The results deriving from the corrected CMs suggest that position information encoded by phase is accurate within 2 by 2 $\bar{m}$ (Fig. 5B, diagonal histograms), and the likelihood of getting a phase readout by chance at this level of accuracy is $P_{\text{subj1}} = 0.0323$ and $P_{\text{subj2}} = 0.0417$. We conclude that in contrast with the heading direction, the position information of the avatar from the phase of spikes is available to neurons downstream, whether it is used.

Comparing position and direction decoding between phase and FR

To assert whether decoding the phase of spikes has any benefit relative to FRs, we compared the position and direction decoding performances of the gamma phase with the decoding from FR. Since the spatial FR distribution of EC grid cells is also spatially periodic, the Bayesian decoding algorithm that we applied to the gamma phase was applicable to FRs with minor modifications. Because unlike phase, FR is bounded to a frequency range between 0 and the maximum FR of the cell, it had to be z-transformed over the area of navigation before using it for decoding. If FR is just as efficient for encoding positions and directions as the phase of firing, then the decoding performance of spike phase could be accounted for by the topography of spike density as opposed to the spike phase relative to LFP. However, the CMs of FR indicated a moderate yet significant decoding power from FR as compared to the gamma phase for both features, allocentric position and allocentric direction in both subjects' data ($\chi^2_{\text{subj1,dir}} = 1.4339$, $P_{\text{subj1,dir}} = 0.2311$; $r_{\text{subj1,dir}} = 0.1356$, $P_{\text{subj1,dir}} = 2.36 \times 10^{-08}$; $\chi^2_{\text{subj1,pos}} = 8.4044$, $P_{\text{subj1,pos}} = 0.0037$; $r_{\text{subj1,pos}} = 0.0235$, $P_{\text{subj1,dir}} = 0.2399$; $t^{\text{subj1}}_{(\text{TP-FP})} = 4.2297$, df = 99, $P = 5.2276 \times 10^{-0.5}$; $\chi^2_{\text{subj2,dir}} = 0.09164$, $P_{\text{subj2,dir}} = 0.7621$; $r_{\text{subj2,dir}} = 0.01262$, $P_{\text{subj2,dir}} = 0.60496$; $\chi^2_{\text{subj2,pos}} = 23.5638$, $P_{\text{subj2,pos}} = 1.2084 \times 10^{-06}$; $r_{\text{subj2,pos}} = 0.0295$, $P_{\text{subj2,dir}} = 0.1390$; tsta $t^{\text{subj2}}_{(\text{TP-FP})} = 2.2087$, df = 99, $P = 0.0295$, where TP and FP denote true positive rate and false positive rate, respectively; fig. S16). The areas under ROC curves (AUC) of position decoding from FR for subjects 1 and 2 were $\text{AUC}_{\text{subj1}} = 0.7072$ and $\text{AUC}_{\text{subj2}} = 0.6150$, respectively, smaller than for gamma phase decoding (fig. S16). In summary, FR provided less information about direction and position of the avatar than the Φ.

DISCUSSION

Spike-LFP phase coherence has been extensively studied within (66–68) and across cortical areas (69). A special class of spike-LFP phase coherence, the theta phase precession, has elucidated the intricate interplay between spikes and the theta oscillation observed in the rodent hippocampus and EC during traversing a place field
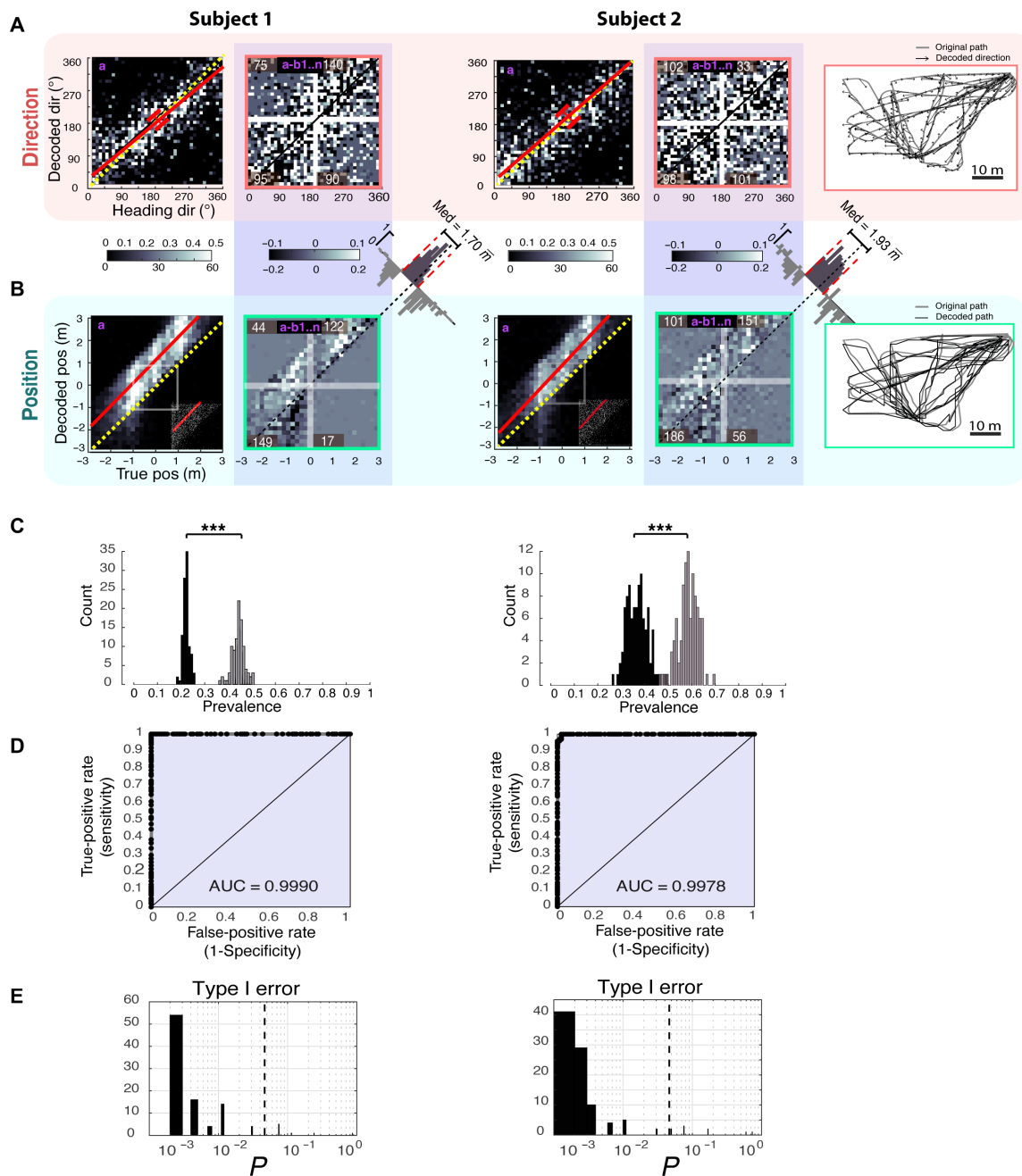
Fig. 5. Bayesian decoding of heading direction and position from the phase of spikes. (**A**) Panels from the left to right are normalized population average of CMs of the decoding of the heading direction before (a) and after trajectory bias correction (a-b), respectively. Left and right blocks represent data (combined across all days, from all environments, and cells) from subjects 1 and 2, respectively. (**B**) Same panels as in (A) except decoding the avatar's position. Possible positions were limited to a 6 by 6 $\bar{\text{m}}$ space. Tilted histograms represent the distributions of position decoding errors (median errors are indicated) with respect to identity lines (dashed line). Insets in (A) represent data points magnified. White numbers are the positive bin counts per quadrant. Trajectory plots at the far right represent single-session examples of direction decoding (top plot) and position decoding (bottom plot). Gray lines are true trajectories, and black arrows and black lines represent the decoded directions and positions, respectively. Examples derived from merging all single units per session in the same environment. (**C**) Histograms show the prevalence of correct position decoding (gray bars) relative to by-chance decoding from phase-shuffled spikes (black bars) for subjects 1 and 2 separately. ***$P < 0.001$. (**D**) ROC curves capture the ratio of spikes correctly decoding the position from phase (true positive) relative to spikes decoding the correct position by chance (false positive). The curve is the aggregate of data points over all experiments grouped by subjects. AUC, area under the curve. (**E**) Distributions of P values of the Kolmogorov-Smirnov tests when comparing the cumulative probability density functions between the observed prediction errors and the errors deriving from 100 shuffled spike phase datasets relative to the identity lines of the CMs. The P values represent the false discovery rate after Benjamini-Hochberg correction. Dashed lines represent the $P = 0.05$ level of confidence.

(*46*, *49*, *70*) as well as in the human hippocampus (*65*). While previous studies have investigated the spike phase within a 1D framework by using linear mazes (*49*), constraining the analysis to omnidirectional passes in open environments (*43*, *71*), analyzing the theta phase during approaching navigational goals (*72*), or predicting trajectories of the animal from 1D theta phase precession of neurons in the CA1 area of the hippocampus and lateral septum (*47*, *48*, *58*), none of these studies extended the scope to reveal the 2D map of spike phase modulation. In contrast, by introducing three manipulations—(i) expressing the same spike phases relative to gamma and theta, (ii) computing the spatial average of phases within 2D environment-aligned bins, and (iii) allowing for 2D navigation—we were able to combine the navigation trajectories into a 2D map and observed grid-like discrete gamma–iso-phase nodes with systematic phase transitions between nodes (Figs. 1, H and J, and 2C and figs. S4 and S11).

By comparing phases of the same spikes when referencing them to gamma versus theta band LFPs, we found that 3 to 10 times as many neurons expressed significant environment-specific phase nonuniformity relative to gamma than to theta (*13*). In addition, gamma phase tuning showed an increased polarization (Figs. 3, A to E, and 4, A to D) relative to theta (Figs. 3F and 4E), and iso-phase node distances in gamma phase were smaller than those constructed from theta (figs. S3, A to D, and S9, E and K), contrary to other approaches focusing only on theta (*18*, *43*, *71*). Not only the gamma phase tuning was more articulated than theta but also the low-frequency components of spatial autocorrelograms computed from gamma phase maps had a larger power than those of theta phase maps. Moreover, the spatial distribution of gamma phase maps, as quantified by entropy, was overall more clustered than that of the theta phase maps (fig. S6, D and E). The enhanced spatial coherence of gamma phase maps relative to the theta phase maps could, at least partly, be accounted to the increased phase variance deriving from the theta phase precession, an explanation that requires further validation.

The third main observation was that the coefficient of variation of population-wide gamma phase modulation was smaller than that of the FR grids' (Fig. 1K), suggesting that the spike phase can encode information under either extremely low or high FR conditions when no grids can be extracted from FRs. This observation was supported by our result showing the immunity of phase maps to ISI shuffling, while the phase randomization of LFP was able to compromise the spike phase maps significantly (fig. S6B) (*13*).

The fourth main observation was that the interelectrode phase shift (Fig. 3, B to E) was consistent with the model of propagating gamma waves (*40*, *67*, *73*), which also can explain why the activities of cells recorded from two adjacent electrodes display a constant phase difference. Moreover, we observed that gamma phases from both multiple neurons recorded from the same electrode and single neurons resulted in discrete multimodal phase distributions (Figs. 3, B to E, and 4, A to D, respectively) (*13*).

Fifth, we demonstrated that both position and direction information can reliably be read out from the phase of spikes (Fig. 5), which raises the intriguing hypothesis that downstream neurons, including pyramidal cells in the hippocampal CA1 and CA3 areas, may be able to decode position and direction information from the phase of action potentials given a shared gamma oscillation, as predicted by the model of gamma phase coding (*45*, *74*).

Last, we showed that gamma phase coding provides a surplus of information relative to the information available from FR alone by comparing the precision by which Bayesian decoding can predict the direction and position of the avatar from FR versus gamma phase (Fig. 5 and fig. S16). We concluded that gamma phase decoding far exceeded the performance of decoding the FR; hence, there must be information contained by the phase that is not available from the FR alone.

The joint representation of direction and location observed in our experiment over the same neuron population is a defining feature of conjunctive cells in layers 3 and 5 of the mEC of the rodent (*75*) with the qualification of head-directional tuning, which should not be confused with the heading direction tuning of phase in our study. However, head direction and heading direction in our experiment were inseparable because the avatar was always facing in the heading direction. Therefore, it is conceivable that a class of grid cells in the human EC also jointly represent direction and location, consistent with reports on goal-specific spike-LFP phase coding found in the human hippocampus relative to theta oscillations (*72*). Although speed was constant in our experiment, location and direction combined with speed could provide a complete positional representation of the agent relative to the navigation space.

In summary, beyond simple phase tuning, we demonstrated a 2D modulation of spike-LFP phase relationship that is (i) periodic in space, (ii) strongest at slow gamma LFP, (iii) persistent, (vi) scales with the environments, (v) allocentric, and (vi) jointly encodes heading direction and relative location. To prove the efficacy of this code, we applied Bayesian decoding on the phases of spikes generated by EC neurons, which demonstrated a reliable readout of positions with a ±1 $\bar{m}$ precision in both x and y dimensions. Given the areas of the mid-size virtual environments (52 by 52 and 50 by 70 $\bar{m}$) and the average seven subdomains within which spike phases uniquely associated with specific locations were observed (i.e., the number of iso-phase nodes), the probability of correctly guessing the location of the impending spike based on the spike phase is less than 0.01, a likelihood worth to consider. To attain this level of confidence, spike phase coding is critically dependent on the frequency and phase of gamma oscillations. On the basis of the dynamic features shared between the human EC neurons and grid cells in the rodent mEC, we posit that the phase of spikes enables the agent to localize itself relative to an allocentric reference frame within the subspace defined by the phase grids with precision exceeding that of FR grids. Whether the two kinds of information encoded by spike phases and FRs are redundant, complementary, or represent disjunct readouts altogether remains to be determined. Regardless of the precise relationship between phase grids and FR grids, the spatial modulation of spike phases by the slow gamma rhythm suggests a new mechanism by which EC acquires stable allocentric representations via the subtle interaction between spiking neurons and the propagating field of gamma oscillation in the human brain.

MATERIALS AND METHODS
Subjects
Two male patients (ages 33 and 40; average, 36 and a half years; Table 1), diagnosed with multifocal epilepsy, were previously consented and implanted with microelectrode arrays in their EC in preparation for surgical resection of epileptic foci. From these two patients (subjects 1 and 2), we could record well-isolated single-unit activity with one channel LFP throughout a 7- and 8-day period in the hospital's epilepsy monitoring unit, while they performed a virtual navigation task that required spatial memory on a tablet computer (Table 1). All surgical and experimental procedures were approved by the Seton Institutional Review Board.

Tasks

The subjects were asked to play a computer game on a tablet they held on their lap. The game's objective was to locate randomly dispersed space aliens in four different environments and return them to preassigned spaceships parking at memorized locations. The four virtual environments included a BY, a courtyard of the LV, a model reconstruction of the main hall of the LX Temple in Egypt, and a large OS with a boundless horizon and minimal external cues (6). These environments differed in several features, including scenery, size, aspect ratio, and presence of obstacles or boundaries (Table 2). The virtual reality environments were designed using Unity 3D (version 3.5.6) and were compiled for Android 4.0. The game rendered the 3D environment from the player's point of view. The player was constrained to the flat ground surface of each map, and their movement speed was a constant 5 $\bar{m}$/s, unless the "GO" button was released or an obstacle inhibited the movement.

Game control

The task was performed on a tablet PC (ASUS Transformer 201 running Android 4.0 at 1280 by 800–pixel resolution). Subjects maneuvered by pressing a GO button with their left thumb and controlled the direction by pressing either a "LEFT" or "RIGHT" button with their right thumb. Before experimental data were collected, subjects were allowed to practice playing the game until they were accustomed to the game controls. The subjects' virtual trajectory and heading (relative to the north-south axis in each game environment) were recorded (6, 13).

Implementation of the task

Our subjects performed virtual spatial navigation tasks implemented as video games using a tablet computer, for a 5- or 10-min duration per game in four different environments (see the "Tasks" section), a total of 40 min/day. The four environments differed in size, geometry, architecture, indoor, outdoor space, and the richness of spatial landmarks (6). The subjects viewed these scenes from the first-person point of view (further referred to as the "avatar's view"). The avatar's movement was controlled by touch screen buttons, allowing movement controls of advancing along a straight or a curved trajectory by pressing GO and/or LEFT or RIGHT buttons at the same time, respectively. The touch screen control enabled also stopping (when not pressing GO) and turning while stopping. The avatar moved by emulating real walking with a constant step size and a constant speed of 1.4 $\bar{m}$/s, where $\bar{m}$ denotes for virtual meter. The objective of the game was to locate randomly placed space aliens, pick them up one by one, and deliver them to one of the two spaceships parked at constant locations within the space. The game program kept track of the avatar's movements with a 16-ms sampling rate synchronized with the display frame rate. The pickup and delivery of a space alien were displayed on the screen giving continuous feedback to the subject on his/her performance. We motivated the subjects to exceed his/her last day's performance. Our subjects were able to complete as many as 50 space alien deliveries per day, with an average of 2 space aliens/min (6, 13).

Synchronizing spatial navigation with neuronal data logging

The subjects' navigation data, recorded on the tablet, was associated with the neuronal data by sending a 25-ms duration frequency-modulated waveform from the tablet's audio output port to the analog auxiliary input port of the data acquisition system each time

the "START" button for the game was released and periodically afterward. The precision of data synchronization between the tablet and the neuronal data logging was <2 ms (SD, 1 ms). This resulted in a spatial localization error of less than 2.5-cm virtual distance (<0.048% of average map width) (6, 13).

Surgical procedures and electrode implantation and explantation

We recorded wide-band signals from no deeper than layers 2 and 3 (given the <0.8-mm tissue penetration and the average 5-mm cortical thickness of human EC, although lacking histological verification) of the mEC. Ad-Tech macro/micro subdural electrodes (catalog code: CMMS-22PX-F478), custom made per our specifications, were surgically implanted in the right hemisphere of two patients. The macro/microelectrode assembly consisted of six macroelectrodes and 16 microelectrode wires arranged in a 4 by 4 grid between the macroelectrodes. The microelectrodes were made of 35-μm platinum-iridium wires arranged in a 4 by 4 wire grid with 1-mm spacing between nearest electrodes. Electrodes were cut to 0.8 mm in length from the electrode base and with a nominal impedance of <3 megohm. Craniotomy and electrode implantation were performed under general anesthesia. After craniotomy, the electrodes were inserted subdurally to the surface of the EC by the neurosurgeon with stereotactic control. The dura was hermetically closed in a watertight fashion, and the bone flap was reattached. The patient remained in the hospital intensive care unit under continuous epilepsy monitoring for 5 to 14 days following the surgery. After sufficient evidence for seizure origin had been collected, electrode explantation and surgical resection of the seizure foci were performed under general anesthesia (6, 13).

Recording neuronal data

Simultaneous single-unit activity was obtained from 5 of 16 microelectrodes at 24-kHz sampling frequency using an FHC Guideline 4000 system, a Food and Drug Administration–approved amplifier for neuronal data acquisition in the human brain. The five electrodes varied across the days and were selected before the recording session based on the largest amplitude and most promising single-unit isolation. The 5- or 10-min traces were bandpass-filtered (300 to 6000 Hz) using a noncausal elliptic filter offline. Because we selected 5 of 16 electrodes with the highest unit activity each day before data logging, we are unable to claim the identity of single units across different days. Simultaneous LFP was sampled from all the five electrodes filtered digitally by a noncausal filter ("filtfilt" function in MATLAB) between 1 and 300 Hz (6, 13).

Spike detection

We applied Wave_clus offline spike detection and spike sorting (76). Spike detection was followed by isolation of single-unit activity using an unsupervised spike-sorting method. For spike detection, we applied a threshold fitted to the median SD of the data (Eq. 1)

$$\text{Thr} = 4\sigma_n; \sigma_n = \text{median}\left\{\frac{|x|}{0.6745}\right\} \tag{1}$$

where x is the bandpass-filtered signal and σ_n is an estimate of the SD of the background noise. In cases when the amplitude threshold did not provide a clear separation between single and multiunit activity, the multiunit activity generated a large "noise

cluster" in the wavelet coefficient space at near-zero amplitude. This isolated noise cluster enabled us to separate single-unit clusters from noise with high confidence. We only included single-unit activity in our dataset if it was separated from the noise cluster by $d > 20$, where d is the Mahalanobis distance (6, 13).

Spike sorting

Spikes different from noise were sorted using the WaveClus method that uses superparamagnetic clustering as a nonparametric classifying engine (76). WaveClus is the second most popular semisupervised method worldwide, used by more than 110 publications, and the most efficient among the bench-marked spike sorting methods (77). The wavelet transform is defined as the convolution between the signal $x(t)$ and a Haar wavelet functions $\psi_{a,b}(t)$

$$W\psi X(a, b) = x(t) \mid \psi_{a,b}(t) \qquad (2)$$

where $\psi_{a,b}(t)$ is dilated (contracted) and shifted versions of a unique wavelet function $\psi(t)$

$$\psi_{a,b}(t) = \mid a \mid^{\frac{1}{2}} \psi\left(\frac{t - b}{a}\right) \qquad (3)$$

where a and b are the scale and translation parameters, respectively. Last, we obtained 12 wavelet coefficients and reduced those to four dimensions with the highest multimodality and deviation from normal distribution. These were the dimensions best discriminating the spikes in wavelet coefficient space. Each spike was associated with a combination of these k most informative wavelet coefficients and hence represented by a point in the k-dimensional space. The data using superparamagnetic clustering resulted in clusters associated with spikes of similar waveforms, where $k = 12$ for all present datasets. The spike times of classified waveforms were tested against 4-ms refractoriness before being associated with putative neurons. We only included neurons where the Mahalanobis distance between the centroid of the noise cluster and the elements of a single-unit cluster or between the centroid of a given single-unit cluster and the elements of another cluster was $d > 20$. We refer to these single-unit clusters as the activity of putative "neurons" (Fig. 1A). Spike times were rounded to the nearest 1-ms interval and expressed in 1-ms precision (6, 13).

Computational methods
Characterizing the avatar's movement in space
The subject's task in the game was to navigate the avatar to pick up randomly displaced space aliens and reach memorized targets with them. During the navigation, some areas were visited more often than others, resulting in an inhomogeneous distribution of sampling of the environment. The $\bar{v}_{(x,y)}$ expressed the distribution of direction crossing at (x,y) area of the environment. The map of directions $\bar{v}_{(x,y)}$ and the RVL ($\sigma \bar{v}_{(x,y)}$) quantified the avatar's movement in four dimensions as the X-Y location, the mean heading direction $\bar{v}_{(x,y)}$ (angle), and the RVL of heading direction $1/\sigma \bar{v}_{(x,y)}$ (the inverse of the variance of directions), given that the avatar was moving with a constant speed. The mean heading direction quantified the angular mean direction of all pathways taken by crossing a unit area regardless of the uniformity of directions, whereas the RVL quantified the unidirectionality of those crosses (6, 13).

Computing heading direction and resultant vectors
The X-Y coordinates of the avatar's movements and heading directions in the environments were up-sampled to 1 kHz by cubic spline interpolation to match with the temporal resolution of neuronal data. Data synchronization was achieved through audio trigger pulses generated by the tablet and recorded through an analog auxiliary input of the data acquisition computer [for method details, see (6)]. From the positions and facing directions (in angular degrees), we constructed a probability density of visits over each unit area of an environment during each game. For the construction of these maps, we divided each environment uniformly by a square grid that was proportional to the size of environments (0.7 m̄ by 0.7 m̄ for the small BY, 2 m by 2 m for the large LX and LV, and 3 m by 3 m for the largest OS environments). Next, we determined the total amount of time spent in each square area, the number of crossings in that area, the circular mean direction of movement $\bar{\omega}_k$ from a set of vectors representing the avatar passing through at a given ij unit area, and the resultant vector of all passes. The length of the resultant vector served as an estimate of the consistency of heading directions over an area. Conversely, the inverse of the RVL described the variance of directions of passing. The average direction $\bar{\omega}_{ij} = 1/N \sum_{k=1}^{N} \omega_k$ was defined as the mean direction of vectors at a given unit area. The mean direction informed us how stereotypical the view was from that location, and the RVL informed us directly about the variance of the directions the avatar took by crossing the place. Given the average constant speed of the avatar, a small resultant vector m_{ij} indicated a large variance of directions, while large m_{ij} implied consistent directions. Direction and resultant vectors were all normalized by the number of vectors in the area. Four types of correlations with phase of spikes were computed: (i) circular correlation between phase angles and motion direction angles (78), (ii) circular to linear correlation between the spike phases and RVL, (iii) independence of spike phase and motion direction distributions vectors using χ^2 tests, and (iv) independence of spike phase and RVL distributions using χ^2 tests (6, 13).

Circular to linear correlation between spike phase and movement resultant vectors
To correlate the average neuronal activity (FRs or spike phases) with movement parameters (heading direction or resultant vector) at any spatial location, we counted the spikes and trajectory segments over small areas each environment was divided into. All trajectory segments crossing a given area were aggregated, and average direction and resultant vectors were computed. Likewise, all spikes within that area were aggregated, and the mean circular phase of spikes was computed. Next, we computed the correlation between mean spike phases and the RVL as circular to linear correlation (78). If our data consist of n pairs of movement velocity (m_{11}, m_{12}, m_{1n}) and spike phase angle (a_{21}, a_{22}, a_{2n}), then the circular correlation is defined (79).

$$r_c l = \frac{\sum_{k=1}^{n} (\sin(\bar{\omega}_{1k}) - m_{1,1})(\sin(\bar{\omega}_{2k}) - m_{2,1})}{\sqrt{\sum_{k=1}^{n} (\sin^2(\bar{\omega}_{1k}) - m_{1,1})(\sin^2(\bar{\omega}_{2k}) - m_{2,1})}} \qquad (4)$$

Correlation between movement direction and spike phase
Let assume our data consist of n pairs of movement angular velocity ($\omega_{11}, \omega_{12}, \omega_{1n}$) and spike phase angle ($\omega_{21}, \omega_{22}, \omega_{2n}$). The circular correlation is defined (79, 80).

$$r_c = \frac{\sum_{k=1}^{n} \sin(\bar{\omega}_{1k} - \Omega_{1,1}) \sin(\bar{\omega}_{2k} - \Omega_{2,1})}{\sqrt{\sum_{k=1}^{n} \sin^2(\bar{\omega}_{1k} - \Omega_{1,1}) \sin^2(\bar{\omega}_{2k} - \Omega_{2,1})}} \tag{5}$$

where $\Omega_{1,1}$ and $\Omega_{2,1}$ are the grand mean direction of the movements and spike phases, respectively. The estimated P value associated with the correlation is based on the assumption that z_r is distributed as standard normal

$$z_r = r_c \sqrt{\frac{n \lambda_{20} \lambda_{02}}{\lambda_{22}}} \tag{6}$$

and

$$\lambda_{ij} = \frac{1}{n} \sum_{k=1}^{n} \sin^i(a_{1k} - T_{1,1}) \sin^j(a_{2k} - T_{2,1}) \tag{7}$$

where $T_{1,1}$ and $T_{2,1}$ denote appropriate angular sample means.

Binning the space for FR maps and phase maps

To elucidate the spatial aspect of spike phase (ϕ), the navigation arena was divided into uniformly sized (1 m by 1 m, 2 m by 2 m, or 3 m by 3 m) squares (unit areas) proportional to the total area of the environment. The size of the unit area did not influence the results within a range of 0.5 m by 0.5 m to 3 m by 3 m (6). For each of those areas, we determined the times of visiting and the number of spikes generated inside the area. The computation of FR maps and phase maps is described in the "Computing spike to LFP phase" and "Spatial FR maps" sections, respectively (13).

Computing 2D entropy

Instead of using traditional grid-score metrics (81, 82), we used entropy for comparing phase maps of original spike trains with surrogate spike and LFP processes [(13). The advantage of entropy over gridness is that it is (i) more general than gridness; (ii) less sensitive to specific features such as rotational symmetry; (iii) agnostic to the grid distance and rotation symmetry unlike gridness, while it is still sensitive to the periodic structure of the 2D image; and (iv) easy to interpret and straightforward to compute. If $p(z_i)$ is the gray-level histogram of the phase map, then the entropy of the image is (83)

$$e - \sum p(z_i) \log_2 p(z_i) \tag{8}$$

Analysis of grid parameters

FR maps, spatial autocorrelograms (ACs), and autoperiodograms were computed using standard methods (6, 75, 81, 82, 84). We quantified grid scores by precisely following the method outlined by Barry and Bush (81), Sargolini et al. (75), and Krupic et al. (82). Grid distance was determined on the basis of the autoperiodogram and manually cross-validated with the ACs. To compute the confidence intervals for statistical significance of gridness scores, we applied a standard Poisson bootstrap method and shuffled spike times 1000 times (not to be confused with the method of generating surrogate spike trains for phase maps in the "Generating surrogate spike trains" section). Validation of spatial periodicity against the by-chance was done using a Monte Carlo method by comparing the spectral modulation depth of each AC against the distribution of gridness scores of 1000 randomized AC generated from mixtures of 2D Gaussian distributions (6, 13).

Computing the FR grid period (grid distance)

Grid period is the wavelength of the spatially periodic single-unit activity. It is equivalent with distance between adjacent nodes of the AC. Since ACs are periodic by construction, this spatial wavelength is defined as the inverse of the predominant spatial frequency component and could also be measured by hand as the average grid distance (2). Grid distances were measured following the method outlined in Nadasdy et al. (6). Briefly, after the removal of the central peak from the AC (nonspecific to the spatial pattern), we computed the 2D spectral density of the ACs by taking the complex conjugate of the inverse 2D Fourier transform (82). We next averaged the 2D spectral distribution across the X and Y coordinates and determined the largest amplitude peak positions. The peak position corresponds to the predominant spatial frequency component of the grid. This method was chosen because it is more precise and less biased than measuring the distance between the nodes by hand. Dividing the dimensions of the AC by the spatial frequency provided the distance of the X-Y peak in spatial bins. We then computed the Euclidean distance of the peak (defined by its X and Y coordinates) from the origin, the center of the autoperiodogram. This distance was multiplied by the scalar bin size (in meters) to give the main grid period λ. Grid frequencies were computed for ACs generated by each neuron and compared between environments. Not to confuse the FR grid distance with the "grid phase node distances" (described in the "Computing grid iso-phase node distance" section) (6, 13).

Computing grid iso-phase node distance

In the lack of a standard method for quantifying the spatial distribution of spike phases projected onto a 2D plane, we applied a manual method. First, we plotted the color-coded phase maps for every single unit that exceeded an average FR of 1 Hz, providing $n \geq 300$ spikes during a 5-min navigation session. The justification for the 1-Hz FR threshold was empirical, as it provided the sufficient coverage for generating continuous phase gradients and discernible iso-phase nodes, i.e., areas where the same phase repeats. We calibrated each phase map according to the size of the virtual environment and digitized the position of iso-phase nodes relative to the edges of the environment. Defining iso-phase nodes started with dividing the phase spectrum to four equal segments (1° to 90°, 91° to 180°, 181° to 270°, and 271° to 360°) corresponding roughly to blue, red, yellow, and green colors of the hue, saturation, value (HSV) color map. Next, we asked unbiased volunteers to mark the centroids of areas on the phase maps where one of the four colors is represented by at least three connected pixels and enter the coordinates into separate spreadsheets. To avoid a bias, the volunteers were blinded to the purpose of the study and the goal of measurements. Once the phase maps were digitized, we computed the Euclidean distances between each node (N) of the same color and determined the inter node distances between them. The total number of distances within an iso-phase node graph is $N = \frac{n*(n-1)}{2}$. Next, we constructed the distribution of these distances. For a periodic graph, the distribution of internode distances formed several prominent peaks with subharmonics. The first peak in the distribution provided the average nearest neighbor internode distance [$\bar{d}$; the mean of $\bar{d}$ across the four phase ranges (color) was used to express the iso-phase distance ($\bar{D}$)] (13).

Datasets and statistical methods

To compare grid scores and grid periods across environments, the general linear model ANOVA and its nonparametric version the Kruskal-Wallis test (MATLAB, MathWorks, Nattick, MA) were applied. The main factor was the environment (BY, LV, LX, and OS),

and the dependent variables were grid period and phase internode distance (*6, 13*). We performed Rayleigh tests for testing nonuniformity of circular data and Watson's goodness of fit test for testing conformity with the von Mises distribution [MATLAB Circular Statistics Toolbox (*78*)].

Processing LFPs

Wide-band signals were recorded from all five electrodes, but we computed the phase of single-unit activity relative to the LFP from only a single dedicated electrode, referred to as El 5. For this electrode, we down-sampled the original wide-band recording from 24 to 1 kHz and digitally filtered the LFP between 1 and 300 Hz for broad spectrum overview using a noncausal, zero phase digital filter implemented in MATLAB as filtfilt (www.mathworks.com/help/signal/ref/filtfilt.html). LFP was then further filtered at specific frequency bands by also using filtfilt for theta (2 to 12 Hz) and gamma (25 to 35 Hz). These frequency intervals were determined on the basis of the prominent frequencies of the fast Fourier transform (FFT) (Fig. 1B). We selected epochs for the phase analysis when the spectral density function at theta or gamma band deviated by ± 2 standard deviations from the $1/f$ regression. Hence, the number of epochs included in the theta and gamma phase analysis differed (*13*).

Computing spike to LFP phase

To get a precise phase estimate of the spikes, we sampled the spike waveform at a 24-kHz sampling rate. We determined the spike time based on the largest first derivative of the positive going component of action potentials. This time point was then rounded to the nearest 1-ms scale and associated with the LFP also sampled at 1 kHz. Next, to obtain the instantaneous phase, the Hilbert transforms of both theta and gamma frequency-filtered signals were computed using the "hilbert" function of MATLAB (www.mathworks.com/help/signal/ref/hilbert.html). The Hilbert phase at spike times (both defined at 1-ms precision) served as instantaneous phase estimate of spike relative to the theta or gamma oscillation (*13*).

Spatial FR maps

The spatial tuning of single-unit activity was characterized by FR maps and their spatial autocorrelation functions. For the FR map, the game area was divided into 1 m–by–1 m, 2 m–by–2 m, or 3 m–by–3 m spatial bins, depending on the size of the virtual environment (Table 2). For each of those spatial bins, we determined the duration of time spent and the number of spikes generated during crossings. By normalizing the number of spikes by the time spent, we obtained the FR in spikes per second (in Hertz). Binning had no significant effect on the grid parameters (*6, 13*).

Computing phase maps

Besides the local FRs, the circular average phase of spikes (ϕ) relative to the theta and gamma bandpass-filtered LFP was computed. Because the frequency of visits varied area to area, including no visit at all, the reliability of (ϕ) estimate also varied with the number of visits. Therefore, we computed the mean and variance (σ^ϕ) of the phase estimate for each area. By spatially integrating the local phase estimates, we constructed a global map ($\hat{\sigma}_\phi$), where the mean phase estimate [$\hat{\phi}_{(x,y)}$] at any given area was associated with a color of the HSV color cylinder (red = −π, green = 0, and red = π), while [$\sigma^\phi_{(x,y)}$] was represented by the value ($\sigma_{max} = 2\pi$ = black and $\sigma_{min} = 0$ = maximum hue) (Figs. 1H and 2C). We refer to the variance-weighted spatial distribution of a phase plot as phase map denoted by (Φ) (*13*). The variance-weighted representation of phase is equivalent to the resultant vector of spike phase (*48*).

Computing autocorrelation

To compute the autocorrelation, the FR map was first smoothed with a Gaussian filter [5 by 5 bin neighborhood, (σ = 0.8)], and nonvisited bins, originally assigned with NaN, were replaced by FR = 0 spikes/s. Autocorrelograms were computed as follows. Given that the original FR map is f and the number of overlapping bins between the original and shifted FR maps at a given τ_x, τ_y offset is n, the equation for the 2D discrete autocorrelation is as follows

$$r(\tau_x, \tau_y) = \frac{n\sum f(x,y)f(x-\tau_x, y-\tau_y) - \sum f(x,y)f(x-\tau_x, y-\tau_y)}{\sqrt{n\sum f(x,y)^2 - (\sum f(x,y))^2}\sqrt{n\sum f(x-\tau_x, y-\tau_y)^2 - (\sum f(x-\tau_x, y-\tau_y))^2}}$$

(9)

where $r(\tau_x, \tau_y)$ is the autocorrelation. Correlations were estimated for all values of n. The central peak of the autocorrelogram was removed before computing the gridness (*84, 85*).

Computing grid scores

We quantified canonical "gridness" based on the autocorrelograms (ACs) by computing a 60° gridness score (**g**) step by step following the exact procedure outlined by Barry and Bush (*81*), Sargolini *et al.* (*75*), and Krupic *et al.* (*82*) as described in our earlier study (*6*). We first normalized the FR maps by the sizes of environments that allowed for equal spatial resolutions for the ACs of different environments, but we kept the aspect ratio differences. Next, we computed the 2D ACs by applying 2D cross-correlation to the FR maps (*6*). After centering and clipping the AC to a 100 by 100 matrix, we located the largest peak after the removal of central peak, which defined a concentric ring containing the circular or ellipsoid arrangement of the first set of autocorrelation peaks at radius R. The outer radius of the ring was, based on the Barry-Krupic (BK) method, chosen to be 2.5R (*6, 13, 75, 81, 82*). For the computation of gridness scores, we followed the method by Sargolini *et al.* (*75*). Accordingly, we filtered the AC with the above-defined ring. Then, we rotated the extracted ring from 1° to 180° and computed the Pearson's correlation coefficients $\bar{r}_{(1°...180°)}$ between the original and rotated matrix with an eight-point moving average applied to it. We determined gridness **g** as the difference between the minimum of $r_{60°}$ or $r_{120°}$ and the maximum of $r_{30°}$, $r_{90°}$, or $r_{150°}$. This function of gridness assumed a 60° modulation of AC as it expresses the modulation depth relative to 60° rotation symmetry. Because r modulation extended between 0 and 1, therefore, **g** was also bounded between 0 and 1.

Generating surrogate spike trains

For testing the deterministic spike-LFP phase relationship against by-chance phase coincidences, we generated surrogate spike trains. To preserve the ISI statistics of the original spike train yet decouple spike times from the phase of LFP, we resampled the ISIs from the ISI histogram and distributed them randomly during the interval of the LFP. We refer to this surrogate as "ISI shuffling." The first ISI of the original spike train was considered relative to time 0. ISI shuffling provided a Null to test the topographical consistency of spike-LFP phase relationship. We reasoned that if the observed spike-LFP phase coupling is topography preserving, then randomizing the phase relationship while retaining the statistics of both ISIs and LFP should lead to a dispersion of topography. Phase topography preservation was tested by cross-validation (see the "Testing the consistency of phase topography by cross-validation" section). Even if spike trains were highly periodic (with a narrow ISI histogram) and potentially increase the by-chance phase coupling between spikes

and LFP, the ISI shuffling would retain that by-chance coupling. In addition, to test whether periodic spike processes are sufficient to model the observed spike to LFP phase relationship, we created spike trains with uniform ISIs by determining the average ISI ($1/f$) and distributed the same number of spikes evenly within the recorded interval. Because trajectories were controlled by the nondeterministic placements of navigation targets, we can rule out any systematic or periodic coupling between the avatar's positions and spike processes. Hence, the periodic spike processes alone cannot account for topography-preserving spike-LFP phase relationship (*13*).

Generating surrogate LFP

Testing the deterministic contribution of LFP to the observed spike to LFP phase relationship, we generated LFP surrogates by phase randomization of the LFP. We applied a phase decomposition of the original LFP, which preserved the original power spectral density, except that the phases of oscillatory components were randomly shifted relative to the original. If spike processes were coordinated with the phase of any LFP component, then that relationship was dissolved by phase randomization. As a result, the observed topographic structure of spike to LFP phase relationship should have been compromised in the surrogate. To remove the low-frequency coherence between spikes and LFP, we reversed the phase-randomized LFP in time. As a result, the phase-randomized and time-reversed LFP should destroy any systematic phase relationship between spikes and LFP (*13*).

Comparing phase maps of original to surrogate spike and LFP

We compared the original (Φ) with those of constructed from surrogate spike trains and surrogate LFP with respect to (i) correlation of phase $\phi_{(x, y)}$ and variance of heading direction [$\sigma \bar{v}_{(x,y)}$] (the inverse of RVL), (ii) grid entropy, and (iii) the power of the low-frequency components of the autocorrelation of (Φ). Statistics were summarized in Table 4. While random LFP phases significantly decreased the covariance of local spike phase with the RVL [$zval^{\text{subj1}} = 10.5241$, $P_{(n = 910)} = 0.0$ and $zval^{\text{subj2}} = 7.8262$ $P_{(n = 1004)} = 0.0$], ISI permutation did not [$zval^{\text{subj1}} = -0.6207$, $P_{(n = 910)} = 0.5348$ and $zval^{\text{subj2}} = 0.2321$, $P_{(n = 1004)} = 0.8165$] (fig. S5A). Similarly, random LFP phase increased the entropy of (Φ), while ISI permutation did not [$zval^{\text{subj1}} = 0.3204$, $P_{(n = 910)} = 0.7487$ and $zval^{\text{subj2}} = 0.9118$, $P_{(n = 1004)} = 0.3619$] (fig. S5B). Moreover, the original (Φ) patterns displayed a significantly larger low-frequency power of the 2D Fourier transform of phase maps than the ISI-shuffled and phase-randomized LFP [ISI shuffling: $zval^{\text{subj1}} = 2.6879$, $P_{(n = 697)} = 0.0072$ and $zval^{\text{subj2}} = 11.8777$, $P_{(n = 1004)} = 0.0$; phase-randomized LFP: $zval^{\text{subj2}} = 8.6097$, $P_{(n = 1004)} = 0.0$], except subject 2 for LFP phase randomization [$zval^{\text{subj1}} = 1.6668$, $P_{(n = 697)} = 0.0956$] (fig. S5C).

Testing the consistency of phase topography by cross-validation

To test for temporal stability, we split a 300-s spike and LFP data into two nonoverlapping 150-s duration epochs and computed an element-to-element correlation between the phase maps (fig. S4, A to D). We excluded the nonvisited areas from the correlation that would otherwise generate spurious correlation. For the 2D cross-correlation, we applied Pearson's correlation between the two vectorized maps following 2D cross-correlation formula

$$r(A, B) = \frac{1}{N-1} \sum_{i=1}^{N} \left(\frac{A_i - \mu_A}{\sigma_A} \right) \left(\frac{B_i - \mu_B}{\sigma_B} \right) \qquad (10)$$

where $r(A, B)$ is the cross-correlation; A and B were matrices representing the two phase maps; μ_A and σ_A are the mean and SD of A, respectively; and μ_B and σ_B are the mean and SD of B. For circular correlation, the same formula was used as above except that (ω_{11}, ω_{12}, ω_{1n}) and (ω_{21}, ω_{22}, ω_{2n}) are the gamma phases of corresponding elements in the two matrices μ_A and μ_B representing the means and σ_A and σ_B were the variance of A and B matrices, respectively (*79*).

For testing the robustness of the spike-gamma phase association, first, we eliminated the odd numbered spikes followed by the even numbered spikes and then constructed phase maps A and B. First, we eliminated the odd numbered spikes, then the even numbered spikes second, and then constructed phase maps A and B (fig. S4, A and E to G). Next, we computed the element-wise 2D correlation coefficients between the two matrices, similar to what we did to the split-half dataset above (*13*).

Generating autocorrelograms of surrogate spike to LFP phases

The topographic maps of spike to LFP phase relationship are affected by the inhomogeneous coverage of space by the time-limited navigation, regardless of whether we were using the original spike trains and LFPs or the surrogate counterparts. All reflected the pattern of spatial coverage, hence increased the correlation between original and surrogate patterns (path correlation). To remove the path correlation confound when evaluating the difference between surrogate and original spike and LFP processes, we constructed autocorrelograms between the spike-LFP phase maps. The nonvisited areas of maps were rendered by random phase values, hence resulted in low average correlations, while visited areas reflected true correlations between original spike/LFP and surrogate spike/LFP. We constructed autocorrelograms of true spike to LFP phase maps, surrogate spike to true LFP phase maps, and true spike to surrogate LFP phase maps (*13*).

Computing the speed of propagation of gamma field

We were interested to compute the speed of gamma wave propagation between electrodes. The 4 by 4 microelectrode grid represents 120 ($n = 16 \times 15/2$) speed measurement options between any two electrodes i and j. Given the known electrode grid geometry and interelectrode distances (λ), the frequency of the gamma carrier wave (f_γ), and the time difference of nearest gamma peaks detected on the electrode pair ij, we can compute the local speed of propagation as the fraction of distance over time

$$\bar{v} = \Delta x / \Delta t \qquad (11)$$

where $\Delta x = \lambda$ and $\Delta t = (\phi_i - \phi_j)/2\pi \times 10e^2/f_\gamma$. Given that the gamma spectrum was set to low gamma (between 25 and 60 Hz) and that the nearest interelectrode distance of our microelectrodes was 0.9 mm, the $\phi_i - \phi_j = 60°$, and the speed of propagation was found to be between 0.3241 mm/ms (at 60 Hz) and 0.1350 mm/ms (at 25 Hz), also consistent with the literature (*45*).

Decoding of position and heading direction from spike phase

In preparation for phase decoding, we assume that all spike time data (T) have been converted to spike phase data (ϕ)

$$T_i \Rightarrow \phi_i \qquad (12)$$

It was also assumed that the navigation area was divided into spatial bins as described earlier, except that for all four environments, we used a uniform 2 by 2 m̄ binning of the area. Hence, the notation ij refers to the ith and jth position of the area of navigation. For predicting the next position of the avatar, we used the actual position

at the time of spike (x_{Ti}, y_{Ti}), the phase of the subsequent spike ϕ_{Ti+1}, and the phase probability map Φ (including the variance). To obtain a reliable estimate of the phase distribution in space (Φ) at each visited spatial bin, we combined the spikes across all units and electrodes for given navigation session per day and per environment

$$\phi_{(ij,1...n)} = \frac{\sum_{k=1}^{E} \sum_{l=1}^{N} \phi_{kN+l}}{EN} \tag{13}$$

where E is the number of electrodes and N is the number of units detected from each electrode.

To ensure that the spike pool used for constructing the phase probability map (Φ) was nonoverlapping with the test set, i.e., the spike pool ϕ used for decoding, we used every even and odd numbered spike for the test set and for the phase probability map, respectively

$$\phi \notin \Phi \tag{14}$$

Next, we integrated the phases across spatial bins of ij into a phase probability map by computing the circular average of spike phases Φ

$$\Phi = \int_{i}^{L} \int_{j}^{M} \phi_{(ij,1,3,5...n)} \tag{15}$$

where L and M defines the size of the environment. Next, we computed the von Mises mean of phases in the space over each spatial bin that provided the phase probability map Φ^{prior}

$$\Phi_{ij} = \frac{\sum_{k=1}^{n_{ij}} \phi_{ijk}}{n_{ij}} \tag{16}$$

The Bayesian decoding started by reading the first spike position (x_{T1}, y_{T1}) of the vector of positions and the phase of the second spike ϕ_2 of the phase vector and loading the phase vector of the next 20 ($i = 2...21$) spikes from the average phase map $\Phi_{(2...21)}$ based on their $[x_{(2...21)}, y_{(2...21)}]$ spatial bin coordinates. The upcoming position of the avatar was predicted as the position with the largest Bayesian probability of positions among the next 20 positions. The Bayesian probability of the avatar's position at x,y given that the spike was fired at a phase of ϕ_i was defined as the product of the likelihood of that phase at that location ($\Phi_{x,y}$ and the prior probability of visiting that location divided by the marginal likelihood of that specific phase occur relative to all the phase values)

$$p(x_i, y_i \mid \phi_i) = \frac{p(\phi \mid x_i, y_i) p(x_i, y_i)}{p(\phi)} \tag{17}$$

Since we already computed the phase probability map Φ, the simplified Bayesian probability is the weighted product of Φ and the probability of occupying the x, y position divided by the probability of phase

$$p(x_i, y_i \mid \phi_i) = \frac{p(\Phi_{x,y}) p(x_i, y_i)}{p(\phi)} \tag{18}$$

where ϕ_i was the observed phase of the ith spike and $\Phi_{x,y}$ was the average phase at the (x, y) spatial bin of the environment. The predicted position was the maximum of the Bayesian probabilities among the 20 upcoming spikes

$$(x_i, y_i) = \arg\max(p(x_{(i,...i+20)}, y_{(i,...i+20)} \mid \phi_{(i,...i+20)}) \tag{19}$$

From (x_i, y_i) and (x_{i-1}, y_{i-1}), we computed the direction of heading as

$$\alpha = \mathrm{atan}(x_i - x_{i-1}, y_i - y_{i-1}) \tag{20}$$

The reason we used only 20 as opposed to all of the spikes was that phase maps were periodic; hence, the same phase value could be mapped to multiple spatial locations. The choice of 20 spikes ensured that the Bayesian prediction will find a local solution within the proximity of the previous spike. We always predicted the upcoming position of a spike relative to the actual spike; hence, we were able to generate vectors of heading directions, which were directly compared to the actual heading direction allowing for statistical estimates of the decoding performance to be made (fig. S12, C to F).

Decoding of position and heading direction from FR
While the firing data are prepared differently, ultimate decoding of position and heading direction information from FRs followed the same procedure as from spike phase (see the "Decoding of position and heading direction from spike phase" section). Because spike density for most neurons was sparse as the pyramidal neurons' FR is less than 1 Hz, we first estimated the continuous FR function from the actual spike times by computing the instantaneous FR at the time of spike $\mathrm{FR}_i = (t_i - t_{i-1})/1000$ in hertz and resampled the nonuniform data at 1.0 kHz by the "resample" function of MATLAB (MathWorks, Nattick, MA), which uses a polyphase anti-aliasing filter. Next, we resampled the data again in 100-ms intervals using the Savitzky-Golay filter, a generalized moving average with filter coefficients determined by an unweighted linear least squares regression and a polynomial model of second degree

$$(T_i \implies t_{\mathrm{resampled}} \implies \mathrm{FR}_i) \tag{21}$$

Then, we treated FR_i exactly as ϕ_i and Eqs. 15 to 20 from the "Decoding of position and heading direction from spike phase" section was applied. Note that FR is a bounded variable between 0 and max(FR), as opposed to phase, but the rest of the data analysis and the Bayesian decoding model was agnostic to this difference.

Construction of CMs of position and heading direction from spike phase
To compare predicted position with observed position, and likewise the predicted heading direction with observed heading direction, we computed the CMs. The CMs represent the observed values (position or direction) on the x axis and the predicted values (position or direction) on the y axis. The resulting 2D histograms represent the aggregate of the pairs of the observed and predicted values at the observed (x) and predicted (y) coordinates for each spike. The scale of the heading direction CM was $x = y = [1...360]°$, while the position was $[0...60]$ m̄.

Construction of angular histograms of aggregate difference between the observed and predicted heading directions
The aggregate differences between actual heading direction vectors and predicted direction vectors constructed a von Mises distribution. The mean of the difference was close to zero if the prediction was correct. We also computed the 360° CM between the predicted and observed directions of heading.

Dependency of decoding on the curvature of trajectories

Because the avatar's movement depended on the location of programmed targets, such as the alien and the spaceships, the avatar's trajectory varied between straight lines and sharp turns. Hence, the spatial distribution of the spikes along the trajectory as potential targets of the next move (among the 20 upcoming spikes) was highly sensitive to the curvature. As a result, when the trajectory was close to a straight line, the 20 upcoming spikes, as possible targets, lined up along the trajectory with a relatively small variation in heading directions and a larger variation in position, while the effect of the large curvature trajectory segments was the opposite. Consequently, the curvature affected the prediction error for direction and for position in an opposite fashion. Small curvature made direction errors small and position errors large, owing to the small directional variance and large positional variance of spike scatter along the straight trajectory. Hence, straight trajectories introduced a direction decoding bias during navigation, while highly curved trajectories introduced a position decoding bias. To compensate for these biases without changing the trajectory, we introduced two interventions: to constrain the decoding to mid-range trajectories and to generate a surrogate spike train (Null) as a control spike dataset described below.

Computing path curvatures

Curvature was defined on every P_{i-1}, P_i, P_{i+1} triplet of trajectory as $\kappa_i = 1/R_i$; hence, $R_i = 1/\kappa_i$, where R is the radius as estimated by the circumcenter of the triangle defined by the three points on the osculating circle (by A. Mjaavatten, MathWorks File Exchange). Regarding the curvature constraints on decoding, we selected trajectory segments where the radius of curvature was larger than 0 and smaller than 15 m and performed all the decoding on these segments. This treatment of using paths with middle-range curvatures served to minimize the influence of curvature on the phase decoding.

Construction of the Null spike dataset

To compensate for any behavioral bias, including the trajectory curvature bias, we generated a dataset (Null) that contained the same number of spikes and same time stamps as in the real data except that spike phases were shuffled. The Null dataset eliminated the association between the spike phase and the avatar's location. To obtain an unbiased estimate of the decoding performance from the shuffled phase dataset, we constructed a CM from the Null. The CM depicted the density of combinations of all observed and decoded movement directions in 360° space and position differences relative to the axes of the environment. When we subtracted the Null from the observed CM (Fig. 4, A and B), the difference represented the unbiased CM. We quantified the decoding by the resultant vector of the polar distribution of angle difference between decoded and true angles. Last, we computed the Kuiper two-sample statistic of the original and Null CMs, as well as the correlation and statistical difference between the decoded true positions and positions decoded from the Null dataset.

Determine precision of position decoding

If Δ_{pos} represents the precision of location decoding from phase, A_1, A_2, A_3, and A_4 are the areas of four different environments, and n_{grids} represent the average number of grid nodes, then the $P(dx, dy \mid \phi)$ probability of the location given a specific spike phase is

$$P(dx, dy \mid \phi) = \frac{\Delta_{pos} * 1/4 * (A_1 + A_2 + A_3 + A_4)}{n_{grids}} \quad (22)$$

Because the Δ_{pos} was different for each individual subjects and the rest of the parameters were fixed, the $1/4 * (A_1 + A_2 + A_3 + A_4) = 2857$ and $n_{grids} = 8$, the formula of computing the probability of by chance, i.e., getting the correct location right from a random code is $P(dx, dy \mid \phi) = \Delta_{pos} * 357.1250$.

Statistical evaluation of CMs by χ^2 statistics

We constructed four different CMs for both subjects (a total of eight CMs), representing the direction decoding from phase, position decoding from phase, direction decoding from FR, and position decoding from FR. For a statistical evaluation of these CMs, first, we eliminated the negative values resulted from subtracting the randomized contingency matrices from the original ones

$$CM = \sqrt{(M \circ M)_{ij}} \quad (23)$$

Second, we split the CM into 2 by 2 quadrants (Q_1, Q_2, Q_3, Q_4) and summed the values within each quadrant generating a 2 by 2 contingency table (n_{q1}, n_{q2}, n_{q3}, n_{q4}). Then, the test of independence boils down to a χ^2 statistics. If the decoding of position or direction as an expected variable was independent from the avatar's observed position or direction, then the observed quantities in (n_{q1}, n_{q2}, n_{q3}, n_{q4}) quadrants should be no different from the expected distribution based on the marginal sums. However, if the decoding works and the expected and observed values are concordant, then the diagonal sum (N_B, N_C) should be significantly larger than chance. With the χ^2 test, we computed the probability of rejecting H_0: the independence of true and decoded movement parameters, i.e., position or direction

$$\chi^2 = \sum_{k=1}^{n} \frac{(O_k - E_k)^2}{E_k} \quad (24)$$

where O_k is the observed and E_k is the expected value in the kth quadrant ($n = 4$). We remark, while χ^2 test quantitatively confirmed the visual observation of the CMs, the 50 by 50 CMs contain much more information than that captured by the 2 by 2 χ^2 test.

Statistical evaluation of CMs by Kolmogorov-Smirnov test

To compare the true CMs with the CMs obtained from the Null dataset, we used the Kolmogorov-Smirnov tests. The Kolmogorov-Smirnov test computes the distance between the two cumulative probability distributions of the two samples and tests the Null hypothesis that the two samples were drawn from the same distribution against the alternative that they are not

$$D^* = \max_x (|\hat{F}_1(x) - \hat{F}_2(x)|) \quad (25)$$

where $\hat{F}_1(x)$ and $\hat{F}_2(x)$ are the empirical distribution functions representing the proportion of ×1 values less than or equal to x and $\hat{F}_2(x)$ the ×2 values less than or equal to x, respectively. If the D^* statistics is larger than the critical value, then we reject the Null and accept the H_1 that the two samples were deriving from two different distributions. Our hypothesis was that if the phase of spikes is informative about the position of the avatar, then the pairs of decoded and actual positions will distribute near the unity line of the CM, while the phase randomized dataset will distribute broadly. Because we generated 100 Null dataset with randomized phases, we obtained not only one but also the statistics of 100 Kolmogorov-Smirnov tests, the distribution of which was computed as a bar chart of P values.

Statistical evaluation of CMs by ROC test

In addition to χ^2 statistics and Kolmogorov-Smirnov test, we quantified how well an ideal observer would discriminate the decoding performance of spike phase code from the decoding of random (shuffled) phases. If the difference between the two distributions is discernible, then the ROC analysis should be able to determine the specificity and sensitivity of the phase code. First, we partitioned the CM to two areas: (i) the diagonal strip defined as $x = y \pm 2\sigma$, also called the identity line; and (ii) everything else around it. If the spike phase decoder worked perfectly, then all the decoded positions or directions would have concentrated along the diagonal. All other scenarios would generate a dispersion of $x \neq y$ values. Since we subtracted the random phase CM from the true phase CM to reduce trajectory bias, if the decoder was operating by chance, then the diagonal confidence interval would have contained close to equal number of positive and negative values, i.e., values reflecting surplus correct decoding and values where the random spike phases would yield to correct position estimates, respectively. Hence, an excess number of positive values would represent a surplus of correctly decoded directions or positions (fig. S15C). In contrast, the negative values would represent correct by-chance decoding performance from random phase distributions, i.e., the false positives (fig. S15D). Likewise, positive values outside of the confidence interval would represent targets missed by the decoder, while negative values off-diagonal represent correctly undetected targets, i.e., negative surplus values from random phase decoding. To compute the ROC curves and the area under that, we plot the function of the number of $s_{x,y} < 0$ values of false positives (fig. S15D) against the number of correctly decoded direction or position parameters (fig. S15C). If the area under the curve is significantly larger than 0.5, then we have a good reason to believe an ideal observer could easily discriminate between decoding of real location or heading direction from decoding randomized spike phase data. The ROC curve enables us to quantify how an ideal observer would be able to discriminate between the two distributions.

SUPPLEMENTARY MATERIALS

Supplementary material for this article is available at https://science.org/doi/10.1126/sciadv.abm6081

View/request a protocol for this paper from *Bio-protocol*.

REFERENCES AND NOTES

1. L. R. Squire, Memory and the hippocampus: A synthesis from findings with rats, monkeys, and humans. *Psychol. Rev.* **99**, 195–231 (1992).
2. T. Hafting, M. Fyhn, S. Molden, M.-B. Moser, E. I. Moser, Microstructure of a spatial map in the entorhinal cortex. *Nature* **436**, 801–806 (2005).
3. A. D. Ekstrom, J. B. Caplan, E. Ho, K. Shattuck, I. Fried, M. J. Kahana, Human hippocampal theta activity during virtual navigation. *Hippocampus* **15**, 881–889 (2005).
4. J. Jacobs, C. T. Weidemann, J. F. Miller, A. Solway, J. F. Burke, X. X. Wei, N. Suthana, M. R. Sperling, A. D. Sharan, I. Fried, M. J. Kahana, Direct recordings of grid-like neuronal activity in human spatial navigation. *Nat. Neurosci.* **16**, 1188–1190 (2013).
5. Y. Shrager, C. B. Kirwan, L. R. Squire, Neural basis of the cognitive map: Path integration does not require hippocampus or entorhinal cortex. *Proc. Natl. Acad. Sci.* **105**, 12034–12038 (2008).
6. Z. Nadasdy, T. P. Nguyen, Á. Török, J. Y. Shen, D. E. Briggs, P. N. Modur, R. J. Buchanan, Context-dependent spatially periodic activity in the human entorhinal cortex. *Proc. Natl. Acad. Sci. U.S.A.* **114**, E3516–E3525 (2017).
7. J. O'Keefe, J. Dostrovsky, The hippocampus as a spatial map. Preliminary evidence from unit activity in the freely-moving rat. *Brain Res.* **34**, 171–175 (1971).
8. J. S. Taube, R. U. Muller, J. B. Ranck, Head-direction cells recorded from the postsubiculum in freely moving rats. II. Effects of environmental manipulations. *J. Neurosci.* **10**, 436–447 (1990).
9. T. Solstad, C. N. Boccara, E. Kropff, M.-B. Moser, E. I. Moser, Representation of geometric borders in the entorhinal cortex. *Science* **322**, 1865–1868 (2008).
10. A. Tsao, J. Sugar, L. Lu, C. Wang, J. J. Knierim, M. B. Moser, E. I. Moser, Integrating time from experience in the lateral entorhinal cortex. *Nature* **561**, 57–62 (2018).
11. L. M. Giocomo, T. Stensola, T. Bonnevie, T. van Cauter, M. B. Moser, E. I. Moser, Topography of head direction cells in medial entorhinal cortex. *Curr. Biol.* **24**, 252–262 (2014).
12. B. J. Kraus, M. P. Brandon, R. J. Robinson II, M. A. Connerney, M. E. Hasselmo, H. Eichenbaum, During running in place, grid cells integrate elapsed time and distance run. *Neuron* **88**, 578–589 (2015).
13. Z. Nadasdy, Á. Török, T. P. Nguyen, J. Y. Shen, D. E. Briggs, P. N. Modur, R. J. Buchanan, Phase of neuronal activity encodes 2-dimensional space in the human entorhinal cortex. *bioRxiv* , 352815 (2018).
14. L. M. Giocomo, E. A. Zilli, E. Fransen, M. E. Hasselmo, Temporal frequency of subthreshold oscillations scales with entorhinal grid cell field spacing. *Science* **315**, 1719–1722 (2007).
15. T. A. Engel, L. Schimansky-Geier, A. V. M. Herz, S. Schreiber, I. Erchova, Subthreshold membrane-potential resonances shape spike-train patterns in the entorhinal cortex. *J. Neurophysiol.* **100**, 1576–1589 (2008).
16. C. B. Lu, J. G. R. Jefferys, E. C. Toescu, M. Vreugdenhil, In vitro hippocampal gamma oscillation power as an index of in vivo CA3 gamma oscillation strength and spatial reference memory. *Neurobiol. Learn. Mem.* **95**, 221–230 (2011).
17. G. Buzsáki, Theta oscillations in the hippocampus. *Neuron* **33**, 325–340 (2002).
18. J. Jacobs, Hippocampal theta oscillations are slower in humans than in rodents: Implications for models of spatial navigation and memory. *Philos. Trans. R. Soc. Lond. B Biol. Sci.* **369**, 20130304 (2014).
19. H. Zhang, J. Jacobs, Traveling theta waves in the human hippocampus. *J. Neurosci.* **35**, 12477–12487 (2015).
20. B. R. Cornwell, L. L. Johnson, T. Holroyd, F. W. Carver, C. Grillon, Human hippocampal and parahippocampal theta during goal-directed spatial navigation predicts performance on a virtual Morris water maze. *J. Neurosci.* **28**, 5983–5990 (2008).
21. Z. M. Aghajan, P. Schuette, T. A. Fields, M. E. Tran, S. M. Siddiqui, N. R. Hasulak, T. K. Tcheng, D. Eliashiv, E. A. Mankin, J. Stern, I. Fried, N. Suthana, Theta oscillations in the human medial temporal lobe during real-world ambulatory movement. *Curr. Biol.* **27**, 3743–3751.e3 (2017).
22. D. J. White, M. Congedo, J. Ciorciari, R. B. Silberstein, Brain oscillatory activity during spatial navigation:theta and gamma activity link medial temporal and parietal regions. *J. Cogn. Neurosci.* **24**, 686–697 (2012).
23. M. P. Brandon, A. R. Bogaard, C. P. Libby, M. A. Connerney, K. Gupta, M. E. Hasselmo, Reduction of theta rhythm dissociates grid cell spatial periodicity from directional tuning. *Science* **332**, 595–599 (2011).
24. J. Koenig, A. N. Linder, J. K. Leutgeb, S. Leutgeb, The spatial periodicity of grid cells is not sustained during reduced theta oscillations. *Science* **332**, 592–595 (2011).
25. J. R. Hinman, M. P. Brandon, J. R. Climer, G. W. Chapman, M. E. Hasselmo, Multiple running speed signals in medial entorhinal cortex. *Neuron* **91**, 666–679 (2016).
26. A. Fernández-Ruiz, A. Oliva, M. Soula, F. Rocha-Almeida, G. A. Nagy, G. Martin-Vazquez, G. Buzsáki, Gamma rhythm communication between entorhinal cortex and dentate gyrus neuronal assemblies. *Science* **372**, eabf3119 (2021).
27. A. Bragin, G. Jando, Z. Nadasdy, J. Hetke, K. Wise, G. Buzsaki, Gamma (40-100 Hz) oscillation in the hippocampus of the behaving rat. *J. Neurosci.* **15**, 47–60 (1995).
28. L. L. Colgin, T. Denninger, M. Fyhn, T. Hafting, T. Bonnevie, O. Jensen, M. B. Moser, E. I. Moser, Frequency of gamma oscillations routes flow of information in the hippocampus. *Nature* **462**, 353–357 (2009).
29. N. Axmacher, M. M. Henseler, O. Jensen, I. Weinreich, C. E. Elger, J. Fell, Cross-frequency coupling supports multi-item working memory in the human hippocampus. *Proc. Natl. Acad. Sci. U.S.A.* **107**, 3228–3233 (2010).
30. F. Mormann, J. Fell, N. Axmacher, B. Weber, K. Lehnertz, C. E. Elger, G. Fernández, Phase/amplitude reset and theta-gamma interaction in the human medial temporal lobe during a continuous word recognition memory task. *Hippocampus* **15**, 890–900 (2005).
31. M. Hasselmo, C. Bodelon, B. Wyble, A proposed function for hippocampal theta rhythm: Separate phases of encoding and retrieval enhance reversal of prior learning. *Neural Comput.* **14**, 793–817 (2002).
32. U. Rutishauser, I. B. Ross, A. N. Mamelak, E. M. Schuman, Human memory strength is predicted by theta-frequency phase-locking of single neurons. *Nature* **464**, 903–907 (2010).
33. A. C. Heusser, D. Poeppel, Y. Ezzyat, L. Davachi, Episodic sequence memory is supported by a theta-gamma phase code. *Nat. Neurosci.* **19**, 1374–1380 (2016).
34. M. M. Yartsev, M. P. Witter, N. Ulanovsky, Grid cells without theta oscillations in the entorhinal cortex of bats. *Nature* **479**, 103–107 (2011).
35. N. J. Killian, M. J. Jutras, E. A. Buffalo, A map of visual space in the primate entorhinal cortex. *Nature* **491**, 761–764 (2012).

36. A. Alonso, R. R. LlinÁs, Subthreshold Na$^+$-dependent theta-like rhythmicity in stellate cells of entorhinal cortex layer II. *Nature* **342**, 175–177 (1989).

37. R. R. Llinas, A. A. Grace, Y. Yarom, In vitro neurons in mammalian cortical layer 4 exhibit intrinsic oscillatory activity in the 10- to 50-Hz frequency range. *Proc. Natl. Acad. Sci. U.S.A.* **88**, 897–901 (1991).

38. M. Okun, A. Naim, I. Lampl, The subthreshold relation between cortical local field potential and neuronal firing unveiled by intracellular recordings in awake rats. *J. Neurosci.* **30**, 4440–4448 (2010).

39. T. V. Ness, M. W. H. Remme, G. T. Einevoll, Active subthreshold dendritic conductances shape the local field potential. *J. Physiol.* **594**, 3809–3825 (2016).

40. B. Telenczuk, N. Dehghani, M. Le Van Quyen, S. S. Cash, E. Halgren, N. G. Hatsopoulos, A. Destexhe, Local field potentials primarily reflect inhibitory neuron activity in human and monkey cortex. *Sci. Rep.* **7**, 40211 (2017).

41. N. Burgess, C. Barry, J. O'Keefe, An oscillatory interference model of grid cell firing. *Hippocampus* **17**, 801–812 (2007).

42. N. Burgess, Grid cells and theta as oscillatory interference: Theory and predictions. *Hippocampus* **18**, 1157–1174 (2008).

43. J. R. Climer, E. L. Newman, M. E. Hasselmo, Phase coding by grid cells in unconstrained environments: Two-dimensional phase precession. *Eur. J. Neurosci.* **38**, 2526–2541 (2013).

44. A. Jeewajee, C. Barry, V. Douchamps, D. Manson, C. Lever, N. Burgess, Theta phase precession of grid and place cell firing in open environments. *Philos. Trans. R. Soc. B Biol. Sci.* **369**, 20120532 (2014).

45. Z. Nadasdy, Information encoding and reconstruction from the phase of action potentials. *Front. Syst. Neurosci.* **3**, 6 (2009).

46. J. O'Keefe, M. L. Recce, Phase relationship between hippocampal place units and the EEG theta rhythm. *Hippocampus* **3**, 317–330 (1993).

47. D. Tingley, G. BuzsÁki, Transformation of a spatial map across the hippocampal-lateral septal circuit. *Neuron* **98**, 1229–1242.e5 (2018).

48. J. D. Monaco, R. M. De Guzman, H. T. Blair, K. Zhang, Spatial synchronization codes from coupled rate-phase neurons. *PLoS Comput. Biol.* **15**, e1006741 (2019).

49. T. Hafting, M. Fyhn, T. Bonnevie, M. B. Moser, E. I. Moser, Hippocampus-independent phase precession in entorhinal grid cells. *Nature* **453**, 1248–1252 (2008).

50. E. T. Reifenstein, R. Kempter, S. Schreiber, M. B. Stemmler, A. V. M. Herz, Grid cells in rat entorhinal cortex encode physical space with independent firing fields and phase precession at the single-trial level. *Proc. Natl. Acad. Sci. U.S.A.* **109**, 6301–6306 (2012).

51. J. C. Magee, Dendritic mechanisms of phase precession in hippocampal CA1 pyramidal neurons. *J. Neurophysiol.* **86**, 528–532 (2001).

52. A. P. Maurer, B. L. McNaughton, Network and intrinsic cellular mechanisms underlying theta phase precession of hippocampal neurons. *Trends Neurosci.* **30**, 325–333 (2007).

53. N. Burgess, J. O'Keefe, Models of place and grid cell firing and theta rhythmicity. *Curr. Opin. Neurobiol.* **21**, 734–744 (2011).

54. A. Kamondi, L. AcsÁdy, X. J. Wang, G. BuzsÁki, Theta oscillations in somata and dendrites of hippocampal pyramidal cells in vivo: Activity-dependent phase-precession of action potentials. *Hippocampus* **8**, 244–261 (1998).

55. E. Pastalkova, V. Itskov, A. Amarasingham, G. BuzsÁki, Internally generated cell assembly sequences in the rat hippocampus. *Science* **321**, 1322–1327 (2008).

56. C. D. Harvey, F. Collman, D. A. Dombeck, D. W. Tank, Intracellular dynamics of hippocampal place cells during virtual navigation. *Nature* **461**, 941–946 (2009).

57. O. Jensen, J. E. Lisman, Position reconstruction from an ensemble of hippocampal place cells: Contribution of theta phase coding. *J. Neurophysiol.* **83**, 2602–2609 (2000).

58. J. R. Huxter, T. J. Senior, K. Allen, J. Csicsvari, Theta phase-specific codes for two-dimensional position, trajectory and heading in the hippocampus. *Nat. Neurosci.* **11**, 587–594 (2008).

59. C. Guger, T. Gener, C. M. A. Pennartz, J. R. Brotons-Mas, G. Edlinger, S. Bermúdez i Badia, P. Verschure, S. Schaffelhofer, M. V. Sanchez-Vives, Real-time position reconstruction with hippocampal place cells. *Front. Neurosci.* **5**, 85 (2011).

60. E. W. Schomburg, A. FernÁndez-Ruiz, K. Mizuseki, A. Berényi, C. A. Anastassiou, C. Koch, G. BuzsÁki, Theta phase segregation of input-specific gamma patterns in entorhinal-hippocampal networks. *Neuron* **84**, 470–485 (2014).

61. F. Bender, M. Gorbati, M. C. Cadavieco, N. Denisova, X. Gao, C. Holman, T. Korotkova, A. Ponomarenko, Theta oscillations regulate the speed of locomotion via a hippocampus to lateral septum pathway. *Nat. Commun.* **6**, 8521 (2015).

62. O. J. Ahmed, M. R. Mehta, Running speed alters the frequency of hippocampal gamma oscillations. *J. Neurosci.* **32**, 7373–7383 (2012).

63. A. J. Watrous, I. Fried, A. D. Ekstrom, Behavioral correlates of human hippocampal delta and theta oscillations during navigation. *J. Neurophysiol.* **105**, 1747–1755 (2011).

64. P. H. Garthwaite, F. G. Elfadaly, J. R. Crawford, Modified confidence intervals for the Mahalanobis distance. *Stat. Probab. Lett.* **127**, 131–137 (2017).

65. S. E. Qasim, I. Fried, J. Jacobs, Phase precession in the human hippocampus and entorhinal cortex. *Cell* **184**, 3242–3255.e10 (2021).

66. M. Vinck, B. Lima, T. Womelsdorf, R. Oostenveld, W. Singer, S. Neuenschwander, P. Fries, Gamma-phase shifting in awake monkey visual cortex. *J. Neurosci.* **30**, 1250–1257 (2010).

67. M. Besserve, S. C. Lowe, N. K. Logothetis, B. Schölkopf, S. Panzeri, Shifts of gamma phase across primary visual cortical sites reflect dynamic stimulus-modulated information transfer. *PLoS Biol.* **13**, e1002257 (2015).

68. M. Siegel, M. R. Warden, E. K. Miller, Phase-dependent neuronal coding of objects in short-term memory. *Proc. Natl. Acad. Sci. U.S.A.* **106**, 21341–21346 (2009).

69. B. Pesaran, J. S. Pezaris, M. Sahani, P. P. Mitra, R. A. Andersen, Temporal structure in neuronal activity during working memory in macaque parietal cortex. *Nat. Neurosci.* **5**, 805–811 (2002).

70. W. E. Skaggs, B. L. McNaughton, M. A. Wilson, C. A. Barnes, Theta phase precession in hippocampal neuronal populations and the compression of temporal sequences. *Hippocampus* **6**, 149–172 (1996).

71. E. Reifenstein, M. Stemmler, A. V. M. Herz, R. Kempter, S. Schreiber, Movement dependence and layer specificity of entorhinal phase precession in two-dimensional environments. *PLOS ONE* **9**, e100638 (2014).

72. A. J. Watrous, J. Miller, S. E. Qasim, I. Fried, J. Jacobs, Phase-tuned neuronal firing encodes human contextual representations for navigational goals. *eLife* **7**, e32554 (2018).

73. A. Bahramisharif, M. A. J. van Gerven, E. J. Aarnoutse, M. R. Mercier, T. H. Schwartz, J. J. Foxe, N. F. Ramsey, O. Jensen, Propagating neocortical gamma bursts are coordinated by traveling alpha waves. *J. Neurosci.* **33**, 18849–18854 (2013).

74. Z. Nadasdy, Binding by asynchrony: The neuronal phase code. *Front. Neurosci.* **4**, 51 (2010).

75. F. Sargolini, M. Fyhn, T. Hafting, B. L. McNaughton, M. P. Witter, M. B. Moser, E. I. Moser, Conjunctive representation of position, direction, and velocity in entorhinal cortex. *Science* **312**, 758–762 (2006).

76. R. Q. Quiroga, Z. Nadasdy, Y. Ben-Shaul, Unsupervised spike detection and sorting with wavelets and superparamagnetic clustering. *Neural Comput.* **16**, 1661–1687 (2004).

77. J. Wild, Z. Prekopcsak, T. Sieger, D. Novak, R. Jech, Performance comparison of extracellular spike sorting algorithms for single-channel recordings. *J. Neurosci. Methods* **203**, 369–376 (2012).

78. P. Berens, CircStat: A MATLAB toolbox for circular statistics. *J. Stat. Softw.* **31**, 1–21 (2009).

79. S. R. Jammalamadaka, A. SenGupta, *Topics in Circular Statistics [electronic resource]* (World Scientific, 2001).

80. N. I. Fisher, A. J. Lee, A correlation coefficient for circular data. *Biometrika* **70**, 327–332 (1983).

81. C. Barry, D. Bush, From A to Z: A potential role for grid cells in spatial navigation. *Neural Syst. Circuits* **2**, 6 (2012).

82. J. Krupic, N. Burgess, J. O'Keefe, Neural representations of location composed of spatially periodic bands. *Science* **337**, 853–857 (2012).

83. R. C. Gonzalez, R. E. Woods, S. L. Eddins, in *Digital Image Processing Using Matlab* (Gonzalez Woods & Eddins, 2004), vol. 624, pp. 609.

84. M. Migliore, T. M. Morse, A. P. Davison, L. Marenco, G. M. Shepherd, M. L. Hines, ModelDB: Making models publicly accessible to support computational neuroscience. *Neuroinformatics* **1**, 135–140 (2003).

85. M. L. Hines, T. Morse, M. Migliore, N. T. Carnevale, G. M. Shepherd, ModelDB: A database to support computational neuroscience. *J. Comput. Neurosci.* **17**, 7–11 (2004).